

Manuscript Number: RSE-D-19-01943R1

Title: Satellite footprint data from OCO-2 and TROPOMI reveal significant spatio-temporal and inter-vegetation type variabilities of solar-induced fluorescence yield in the U.S. Midwest

Article Type: Research Paper

Keywords: solar-induced chlorophyll fluorescence, OCO-2, TROPOMI, fluorescence yield, croplands, NIRv, escaping ratio

Corresponding Author: Dr. Cong Wang, Ph.D

Corresponding Author's Institution:

First Author: Cong Wang, Ph.D

Order of Authors: Cong Wang, Ph.D; Kaiyu Guan; Bin Peng; Min Chen; Chongya Jiang; Yelu Zeng; Genghong Wu; Sheng Wang; Jin Wu; Xi Yang; Christian Frankenberg; Philipp Köhler; Joseph Berry; Carl Bernacchi; Kai Zhu; Caroline Alden; Guofang Miao

Abstract: Solar-induced chlorophyll fluorescence (SIF) measured from space has been increasingly used to quantify plant photosynthesis at regional and global scales. Apparent canopy SIF yield (SIF_{yield} apparent), determined by fluorescence yield (ΦF) and escaping ratio (fesc), together with absorbed photosynthetically active radiation (APAR), is crucial in driving spatio-temporal variability of SIF. While strong linkages between SIF_{yield} apparent and plant physiological responses and canopy structure have been suggested, spatio-temporal variability of SIF_{yield} apparent at regional scale remains largely unclear, which limits our understanding of the spatio-temporal variability of SIF and its relationship with photosynthesis. In this study, we utilized recent SIF data with high spatial resolution from two satellite instruments, OCO-2 and TROPOMI, together with multiple other datasets. We estimated SIF_{yield} apparent across space, time, and different vegetation types in the U.S. Midwest during crop growing season (May to September) from 2015-2018. We found that SIF_{yield} apparent of croplands was larger than non-croplands during peak season (July-August). However, SIF_{yield} apparent between corn (C4 crop) and soybean (C3 crop) did not show a significant difference. SIF_{yield} apparent of corn, soybean, forest, and grass/pasture show clear seasonal and spatial patterns. The spatial variability of precipitation during the growing season could explain the overall spatial pattern of SIF_{yield} apparent. Further analysis by decomposing SIF_{yield} apparent into ΦF and fesc using near-infrared reflectance of vegetation (NIRV) suggests that fesc may be the major driver of the observed -variability of SIF_{yield} apparent.

Highlights

- $SIF_{\text{yield apparent}}$ is interpreted using high spatial resolution satellite footprints.
- Different spatio-temporal patterns of $SIF_{\text{yield apparent}}$ are revealed among vegetation types.
- $SIF_{\text{yield apparent}}$ of croplands is larger than non-croplands in summer.
- Escaping ratio largely explains the variations of $SIF_{\text{yield apparent}}$ in the Midwest.
- Spatial variability of $SIF_{\text{yield apparent}}$ is correlated to precipitation.

Satellite footprint data from OCO-2 and TROPOMI reveal significant spatio-temporal and inter-vegetation type variabilities of solar-induced fluorescence yield in the U.S.

Midwest

Cong Wang^{1*}, Kaiyu Guan^{1,2*}, Bin Peng^{1,2}, Min Chen³, Chongya Jiang^{1,4}, Yelu Zeng⁵, Genghong Wu¹, Sheng Wang¹, Jin Wu⁶, Xi Yang⁷, Christian Frankenberg^{8,9}, Philipp Köhler⁸, Joseph Berry⁵, Carl Bernacchi^{4,10,11}, Kai Zhu¹², Caroline Alden^{13,14}, and Guofang Miao¹

¹ College of Agricultural, Consumer and Environmental Sciences, University of Illinois at Urbana Champaign, USA

² National Center for Supercomputing Applications, University of Illinois at Urbana-Champaign, USA

³ Joint Global Change Research Institute, Pacific Northwest National Laboratory, College Park, MD, USA

⁴ Carl R. Woese Institute for Genomic Biology, University of Illinois at Urbana-Champaign, Urbana, IL, USA

⁵ Department of Global Ecology, Carnegie Institution for Science, Stanford, CA, USA

⁶ Department of Environmental and Climatic Sciences, Brookhaven National Laboratory, Upton, NY, USA

⁷ Department of Environmental Sciences, University of Virginia, Charlottesville, VA, USA

⁸ Division of Geological and Planetary Sciences, California Institute of Technology, Pasadena, CA, USA

⁹ Jet Propulsion Laboratory, California Institute of Technology, Pasadena, CA, USA

¹⁰ Department of Plant Biology, University of Illinois at Urbana-Champaign, Urbana, IL, USA

¹¹ USDA ARS Global Change and Photosynthesis Research Unit, Urbana, IL, USA

¹² Department of Environmental Studies, University of California, Santa Cruz, CA, USA

¹³ Cooperative Institute for Research in Environmental Sciences, University of Colorado
Boulder, Boulder, CO, USA

¹⁴ NOAA/ESRL Global Monitoring Division, Boulder, CO, USA

* Corresponding author: Kaiyu Guan and Cong Wang

E-mail address: kaiyug@illinois.edu (Kaiyu Guan) and wangcongrs@gmail.com (Cong Wang)

1 **Abstract:**

2 Solar-induced chlorophyll fluorescence (SIF) measured from space has been increasingly used
3 to quantify plant photosynthesis at regional and global scales. Apparent canopy SIF yield
4 ($SIF_{\text{yield apparent}}$), determined by fluorescence yield (Φ_F) and escaping ratio (f^{esc}), together with
5 absorbed photosynthetically active radiation (APAR), is crucial in driving spatio-temporal
6 variability of SIF. While strong linkages between $SIF_{\text{yield apparent}}$ and plant physiological
7 responses and canopy structure have been suggested, spatio-temporal variability of SIF_{yield}
8 apparent at regional scale remains largely unclear, which limits our understanding of the spatio-
9 temporal variability of SIF and its relationship with photosynthesis. In this study, we utilized
10 recent SIF data with high spatial resolution from two satellite instruments, OCO-2 and
11 TROPOMI, together with multiple other datasets. We estimated $SIF_{\text{yield apparent}}$ across space, time,
12 and different vegetation types in the U.S. Midwest during crop growing season (May to
13 September) from 2015-2018. We found that $SIF_{\text{yield apparent}}$ of croplands was larger than non-
14 croplands during peak season (July-August). However, $SIF_{\text{yield apparent}}$ between corn (C4 crop)
15 and soybean (C3 crop) did not show a significant difference. $SIF_{\text{yield apparent}}$ of corn, soybean,
16 forest, and grass/pasture show clear seasonal and spatial patterns. The spatial variability of
17 precipitation during the growing season could explain the overall spatial pattern of $SIF_{\text{yield apparent}}$.
18 Further analysis by decomposing $SIF_{\text{yield apparent}}$ into Φ_F and f^{esc} using near-infrared reflectance
19 of vegetation (NIR_V) suggests that f^{esc} may be the major driver of the observed variability of
20 $SIF_{\text{yield apparent}}$.

21

22 **Keywords:** solar-induced chlorophyll fluorescence, OCO-2, TROPOMI, fluorescence yield,
23 croplands, NIR_V , escaping ratio

24

25 **1. Introduction**

26 Accurate and timely estimation of ecosystem photosynthesis measured as gross primary
27 production (GPP) is crucial for understanding carbon exchange between the biosphere and
28 atmosphere (Beer et al., 2010). GPP also largely determines vegetation net primary productivity
29 and crop yield (Guan et al., 2016; Guanter et al., 2014). Satellite measurements of solar-induced
30 chlorophyll fluorescence (SIF) are increasingly used to approximate GPP variability across
31 large spatial and temporal scales (Frankenberg et al., 2011; Guan et al., 2016; Joiner et al., 2011;
32 MacBean et al., 2018; Shiga et al., 2018). A number of studies have shown either linear or
33 nonlinear relationships between GPP and canopy SIF at different spatial and temporal scales
34 and from various sensors (Li et al., 2018a; Smith et al., 2018; Verma et al., 2017; Zuromski et
35 al., 2018; Damm et al., 2015; Zhang et al., 2016). However, fundamental controls of large-scale
36 variabilities in SIF remain unclear.

37 The widely-used light use efficiency (LUE)-based GPP model (Monteith, 1972) can be
38 adapted to express SIF at the top of canopy (Guanter et al., 2014):

$$39 \quad GPP = PAR \times fPAR \times LUE = APAR \times LUE \quad (1)$$

40 and

$$41 \quad SIF = PAR \times fPAR \times SIF_{\text{apparent yield}} \\ 42 \quad = APAR \times SIF_{\text{apparent yield}} = APAR \times \Phi_F \times f^{esc} \quad (2)$$

43 where PAR is photosynthetically active radiation, fPAR is the fraction of absorbed
44 photosynthetically active radiation, APAR is absorbed PAR and LUE is light use efficiency at
45 which APAR is used in photosynthesis. Apparent canopy SIF yield ($SIF_{\text{yield apparent}}$) can be

46 defined as SIF observed in the direction of the sensor per PAR absorbed by canopies. SIF_{yield}
47 $_{apparent}$ is jointly determined by fluorescence yield (Φ_F) and escaping ratio (f^{esc} , Liu et al., 2018;
48 Yang and van der Tol, 2018; Zeng et al., 2019; Du et al., 2017). Empirical studies have reported
49 correlations between LUE and $SIF_{yield\ apparent}$ (Yang et al., 2017; Yang et al., 2015), and linkage
50 between $SIF_{yield\ apparent}$ and plant physiological response (Song et al, 2018). Based on Equation
51 2, both APAR and $SIF_{yield\ apparent}$ contribute to overall SIF variability. Although some studies
52 find a strong dominance of APAR in SIF (e.g. Miao et al., 2018; Yang et al., 2018), SIF_{yield}
53 $_{apparent}$ variation is what distinguishes SIF from APAR. Significant efforts have been made to
54 derive PAR and fPAR from satellite remote sensing and ground-based observations (Ryu et al.,
55 2018; Tian, 2004), yet characterization and understanding of $SIF_{yield\ apparent}$ remain much less
56 studied. Existing studies have shown that $SIF_{yield\ apparent}$ can vary with vegetation type, plant age,
57 growth stage, and growth conditions (Colombo et al., 2018; Miao et al., 2018; Sun et al., 2015).
58 Additionally, there are indications of considerable spatio-temporal variations of $SIF_{yield\ apparent}$
59 (Joiner et al., 2011; Li et al., 2018b). However, understanding of $SIF_{yield\ apparent}$ variability over
60 large spatial and temporal scales is insufficient, and the knowledge gap in $SIF_{yield\ apparent}$ over
61 spatio-temporal scales is an outstanding source of uncertainty that limits our current
62 understanding of SIF variability.

63 Various satellite-based SIF sensors have emerged in the past decade and derived SIF
64 products have progressed from coarse resolutions in space and time to finer resolution. The first
65 global SIF product from Greenhouse Gases Observing Satellite (GOSAT, Frankenberg et al.,
66 2011; Guanter et al., 2012; Joiner et al., 2011), and the subsequent products from Global Ozone
67 Monitoring Experiment-2 (GOME-2, Joiner et al., 2013; Köhler et al., 2015) and SCanning

68 Imaging Absorption spectroMeter for Atmospheric CHartographY (SCIAMACHY, Joiner et
69 al., 2012; Köhler et al., 2015) provide an important opportunity to evaluate $SIF_{\text{yield apparent}}$ over
70 large spatio-temporal scales (Joiner et al., 2011). However, due to coarse resolutions of those
71 SIF products (0.5° or coarser for gridded data) and associated intra-pixel mixing effects, the
72 accuracy of $SIF_{\text{yield apparent}}$ estimation at the vegetation-type level is limited. Launched on July
73 2, 2014, Orbiting Carbon Observatory-2 (OCO-2) retrieves SIF at a significantly improved
74 spatial resolution compared with previous SIF products, though the spatial coverage is sparse
75 (Frankenberg et al., 2014). The spatial resolution of an OCO-2 footprint is approximately
76 $1.3 \times 2.25 \text{ km}^2$. Recent studies have compared and validated OCO-2 SIF products with GPP
77 measurements from eddy covariance (EC) flux towers, given the comparable spatial footprints
78 between GPP and SIF measurements (Li et al., 2018c; Lu et al., 2018). Additionally, a new SIF
79 product based on TROPOspheric Monitoring Instrument (TROPOMI) was released in 2018
80 (Köhler et al., 2018). TROPOMI measures SIF at both high spatial resolution and high temporal
81 frequency, with a footprint of $3.5 \times 7 \text{ km}^2$ at nadir and almost daily coverage. The two high-
82 spatial-resolution SIF datasets, OCO-2 and TROPOMI, have the potential to provide more
83 accurate assessments of $SIF_{\text{yield apparent}}$ for specific vegetation types.

84 The U.S. Midwest Corn Belt currently produces more than 30% of global corn and
85 soybean (USDA, 2018), and has been identified as a global SIF hotspot during the boreal
86 summer (Guanter et al., 2014). Therefore, a better understanding of the controls on SIF would
87 likely lead to a better quantification of regional carbon budgets and improved prediction of crop
88 productivity (Guan et al., 2016). To understand controls of SIF variations, estimating SIF_{yield}
89 apparent for each vegetation type is necessary because $SIF_{\text{yield apparent}}$ can vary substantially

90 between different vegetation types in this area. First, the $SIF_{\text{yield apparent}}$ of croplands is likely
91 larger than that of non-croplands since SIF in the U.S. Corn Belt is remarkably high during crop
92 growing season (Guanter et al., 2014). Second, within croplands, the GPP of corn is usually
93 much larger than that of soybean (Joo et al., 2016; Suyker and Verma, 2012). This difference
94 in photosynthesis could be attributed to canopy structure, for example, leaf area index (LAI)
95 and leaf angle distribution (LAD), and plant physiology, both of which could potentially drive
96 differences in $SIF_{\text{yield apparent}}$ (Frankenberg and Berry, 2018; Porcar-Castell et al., 2014).
97 However, whether and how $SIF_{\text{yield apparent}}$ of corn and soybean differ is still not well studied.
98 Finally, the non-crop vegetation types of forest and grass/pasture, for example, are also different
99 in both physiological processes and canopy structures.

100 This study aims to provide a comprehensive analysis of the spatio-temporal variability of
101 $SIF_{\text{yield apparent}}$ of vegetation in the U.S. Midwest. The two newest satellite SIF datasets, i.e.
102 OCO-2 and TROPOMI footprint SIF observations, are used to provide a more accurate
103 estimation of $SIF_{\text{yield apparent}}$ of specific vegetation types. Specifically, we aim to address the
104 following questions: How does $SIF_{\text{yield apparent}}$ of croplands differ from $SIF_{\text{yield apparent}}$ of non-
105 croplands during crop growing season? How does $SIF_{\text{yield apparent}}$ of corn (C4 crop) differ from
106 $SIF_{\text{yield apparent}}$ of soybean (C3 crop)? What are seasonal and spatial patterns of $SIF_{\text{yield apparent}}$ of
107 the four major vegetation types? What drives variability of $SIF_{\text{yield apparent}}$ in space, time, and
108 across vegetation types?

109

110 **2. Data and Methodology**

111 **2.1 Study region**

112 The study region spans 15 states in the U.S. Midwest region (Fig. 1) including North
113 Dakota, South Dakota, Nebraska, Kansas, Minnesota, Iowa, Missouri, Wisconsin, Illinois,
114 Michigan, Indiana, Ohio, Kentucky, Wyoming (East to 107 °W), and Colorado (East to
115 107 °W). Corn and soybean are the major crop types in this area. In addition to crops, forest
116 and grass/pasture are also dominant vegetation types in the U.S. Midwest. Forests are mainly
117 distributed in the northeast, southeast, and west of the study area and grass/pasture is mainly
118 distributed in the west (Fig. 1). Most forests are temperate deciduous, except for Ponderosa
119 Pine in the west and Spruce/Fir in the north. In this study, we focused on the four main
120 vegetation types: corn, soybean, forest, and grass/pasture.

121

122 **2.2 Satellite SIF footprint data**

123 We primarily used the OCO-2 SIF Lite product (v. B8100r), which contains bias-corrected
124 SIF and other related fields for individual footprints on a daily basis (Sun et al., 2018). The data
125 were obtained from (ftp://fluo.gps.caltech.edu/data/OCO2/sif_lite_B8100/). The OCO-2
126 spectrometer measures high-resolution spectra in O₂-A band (757-775 nm, full width at half
127 maximum = 0.042 nm) with a local overpass time at about 1:30 pm, which was utilized for

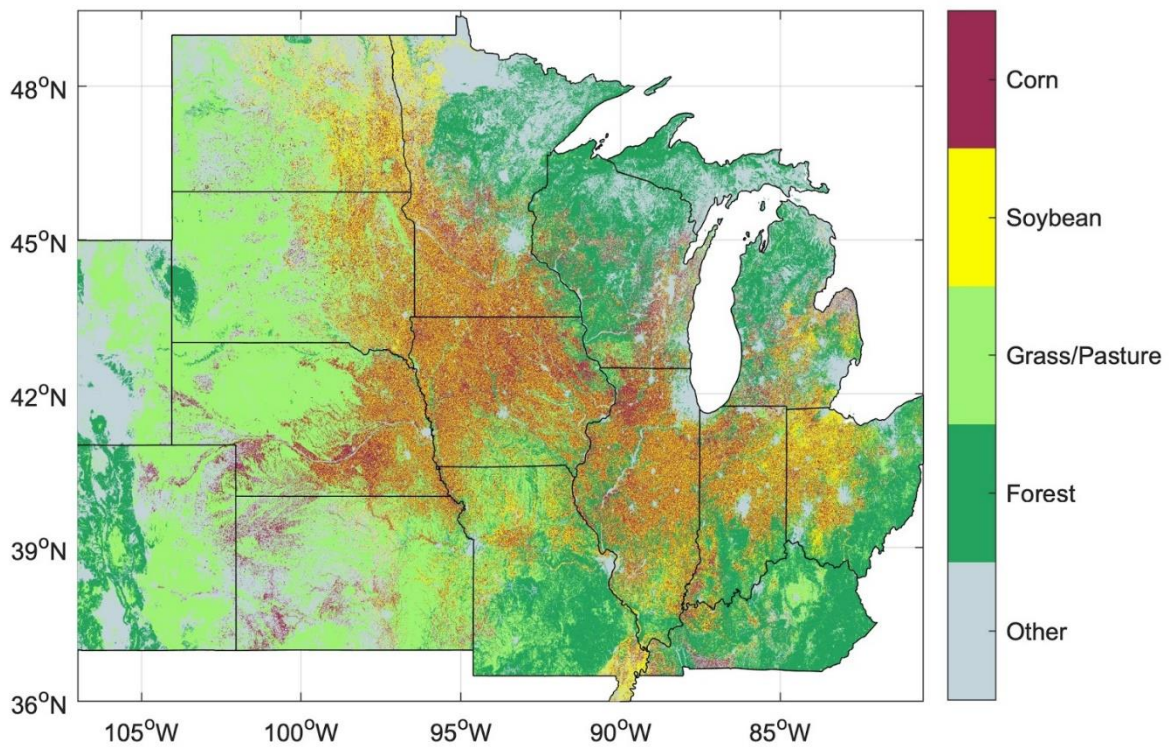


Fig. 1 Main vegetation types (i.e. corn, soybean, grass/pasture, and forest) in the U.S. Midwest, derived from Cropland Data Layer of 2015 for illustration.

128 OCO-2 SIF retrievals at 757 nm (SIF757) and 771 nm (SIF771) based on in-filling of solar
 129 Fraunhofer lines (Frankenberg et al., 2014). SIF values used here were calculated as
 130 $(SIF757 + 1.5 \times SIF771) / 2$ because SIF771 is typically ~ 1.5 times lower than SIF757 (Sun et al.,
 131 2018). The nominal spatial resolution of a footprint is $1.3 \times 2.25 \text{ km}^2$, with eight footprints along-
 132 track covering a 10.6 km-wide swath and a repeat cycle of approximately 16 days. SIF
 133 observations depend on viewing geometry (Z. Zhang et al., 2018) which for OCO-2 alternates
 134 mainly between nadir mode and glint mode. We only used measurements from nadir mode
 135 because of slightly higher spatial resolution, a better signal-to-noise ratio over land and more
 136 useful soundings in regions impacted by clouds and topography (Sun et al., 2018). We used
 137 only data during the crop growing season (May - September) from 2015 to 2018. Fig. 2a and
 138 2b show a summary of the spatial and temporal coverage of OCO-2 footprints used in the study.

139 The footprints were distributed along separated tracks with high data density in the west; fewer
 140 data were available in August and September in 2017.

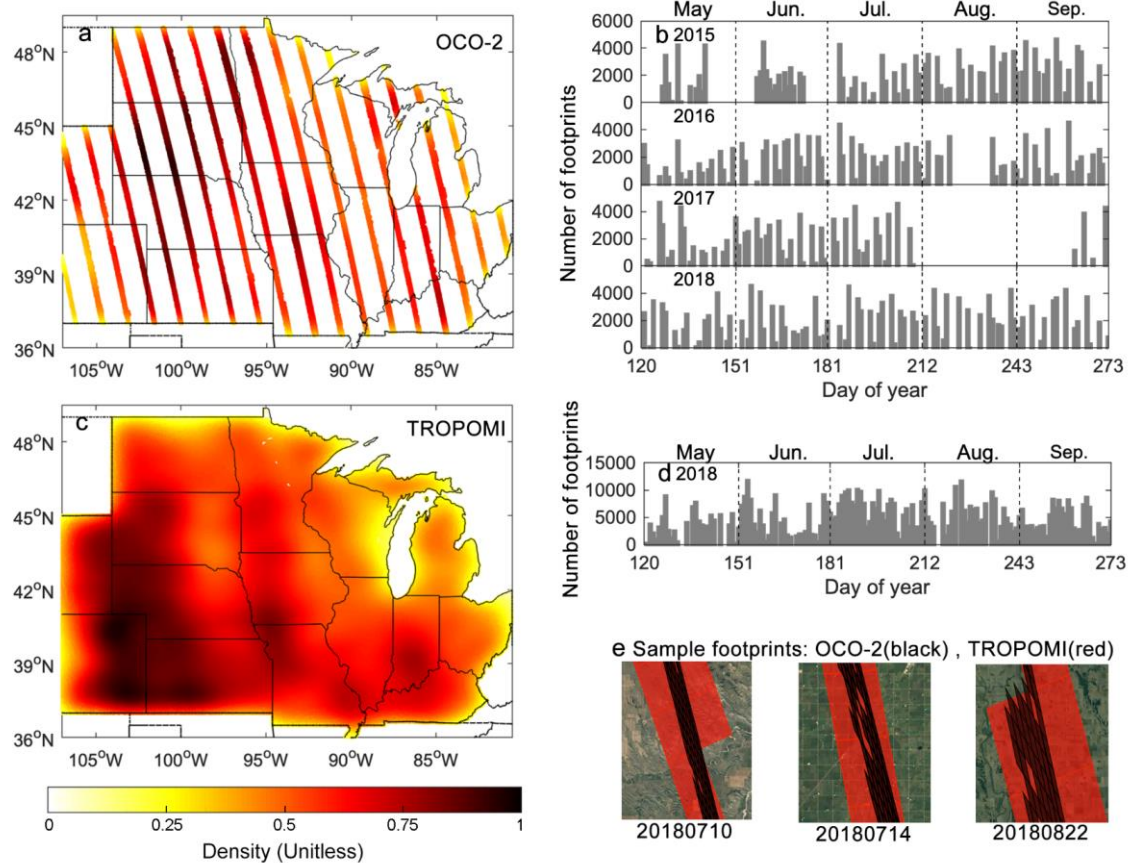


Fig. 2 Illustration of availability of OCO-2 and TROPOMI footprint data in both space and time. Panels (a) and (b) respectively represent the spatial coverage and frequency of observations over time for OCO-2 data from 2015 to 2018. Panels (c) and (d) are the spatial and temporal distributions of the number of the footprint of TROPOMI data in 2018. (e) shows three examples of the footprint of OCO-2 and TROPOMI. The color background shown in (a) and (c) represents the density of the footprint observations.

141 In addition to OCO-2, we also used the latest released TROPOMI SIF footprint data
 142 (<ftp://fluo.gps.caltech.edu/data/tropomi/>). The TROPOMI onboard Sentinel 5 Precursor
 143 satellite has a local overpass time at about 1:30 pm and a repeat cycle of 17 days, and provides
 144 spectra measurements in the near-infrared band (band 6, 727-775 nm, full width at half
 145 maximum = 0.38 nm), which makes SIF retrieval possible. A data-driven approach similar to
 146 previous studies (Guanter et al., 2015; Köhler et al., 2015) was employed to extract the SIF
 147 signal using spectral measurements ranging from 743 nm to 758 nm (Köhler et al., 2018). The
 148 nominal spatial resolution of a TROPOMI footprint is 7 km along track and 3.5-15 km across
 149 track, with a wide swath width of approximately 2,600 km. This wide swath allows almost daily
 150 global observations. We used available data from May to September in 2018 with cloud cover
 151 less than 0.3 and view zenith angle less than 10 degrees. Fig. 2e shows some examples of the
 152 selected TROPOMI footprints. Fig. 2c and 2d show a summary of the spatial and temporal
 153 availability of the total TROPOMI footprint observations used in the current study.

154 **2.3 Estimating $SIF_{\text{yield apparent}}$, Φ_F and f^{esc} at the satellite footprint level**

155 In this section, we describe ancillary data and how we process these data to estimate
 156 $SIF_{\text{yield apparent}}$, Φ_F , and f^{esc} at the satellite footprint level. $SIF_{\text{yield apparent}}$ at the satellite footprint
 157 level is calculated according to Equation 2.

158 Estimating f^{esc} and Φ_F over a large scale is challenging. In this study, we employed the
 159 following equations according to a newly developed algorithm (Zeng et al, 2019):

$$160 \quad f^{\text{esc}} \approx \frac{NIR_v}{fPAR} \quad (3)$$

$$161 \quad \Phi_F \approx \frac{SIF}{PAR \times NIR_v} \quad (4)$$

$$162 \quad NIR_v = NIR \times NDVI = NIR \times \frac{NIR-Red}{NIR+Red} \quad (5)$$

163 where NIR_v is near-infrared reflectance of vegetation, NIR and Red are reflectances of near-
164 infrared and red bands. To calculate these variables, SIF data were obtained from OCO-2 and
165 TROPOMI datasets as described in Section 2.2. Instantaneous PAR is the output product from
166 Ryu et al., (2018). An artificial neural network surrogate model (Ryu et al., 2018), trained from
167 a Monte Carlo ray-tracing model (Kobayashi and Iwabuchi, 2008) was used to produce the
168 product. The model was driven by MODIS cloud optical thickness (3 km resolution), aerosol
169 optical depth (1 km resolution), total water vapor (1 km resolution), total ozone (5 km
170 resolution), and shortwave albedo products (1 km resolution), as well as GMTED2010
171 elevation product (1 km resolution). Detailed information about the model and data processing
172 can be found in Ryu et al. (2018). Four fPAR datasets were used to estimate $SIF_{yield\ apparent}$.
173 MCD15A2H from MODIS (Myneni et al., 2002) and VNP15A2H from VIIRS (Myneni and
174 Knyazkhin 2018) are 8-day composite datasets with a spatial resolution of 500 m. PROBA-V
175 GEOV1 fPAR data are delivered every 10 days with a spatial resolution of 300 m (Baret et al
176 2013). We calculated daily fPAR from the three temporal composited fPAR datasets using a
177 simple linear interpolation. MCD43A4 provides daily Nadir Bidirectional Reflectance
178 Distribution Function (BRDF)-Adjusted Reflectance data at a 500-meter resolution which were
179 used to calculate NDVI. A simple NDVI-fPAR model was employed to generate the fourth
180 fPAR estimation (Peng et al., 2012, Text S1). Only footprints with all the four fPAR values
181 larger than 0.1 were included. $SIF_{yield\ apparent}$ was calculated independently with the four fPAR
182 estimations. The averaged $SIF_{yield\ apparent}$ from the four estimations was finally used in the
183 analysis. MCD43A4 was also used to calculate NIR_v .

184 **2.4 Data analysis**

185 We performed the following analysis to address the scientific questions raised in the
186 introduction section. First, to detect the difference of $SIF_{\text{yield apparent}}$ between croplands (corn and
187 soybean) and non-croplands, we examined relationships between the land cover fraction of
188 croplands and $SIF_{\text{yield apparent}}$ at the satellite footprint level for both OCO-2 and TROPOMI over
189 the entire study domain. The land cover fraction of different vegetation types was calculated
190 from the USDA NASS Cropland Data Layer (CDL) dataset. A linear regression analysis was
191 conducted for each month from May to September. The slope of the regression indicates a
192 difference of $SIF_{\text{yield apparent}}$ between croplands and non-croplands; a positive slope means that
193 $SIF_{\text{yield apparent}}$ of croplands is larger than that of non-croplands. We performed this analysis
194 rather than directly comparing pure croplands and non-croplands footprints because most
195 footprints contain mixed vegetation types.

196 Second, we selected cropland dominated footprints, defined as those footprints with a
197 fraction of croplands greater than 80%. We then examined relationships between corn fraction
198 of the total area in a footprint and $SIF_{\text{yield apparent}}$ to detect the difference of $SIF_{\text{yield apparent}}$ between
199 corn and soybean. An increasing trend of $SIF_{\text{yield apparent}}$ with the increase of corn fraction
200 indicates that the $SIF_{\text{yield apparent}}$ of corn is larger than soybean. The analysis was performed over
201 the entire study area and also over three small sub-regions.

202 Spatial-temporal patterns of $SIF_{\text{yield apparent}}$ of different vegetation types were explored.
203 Both f^{esc} and Φ_F can contribute to the spatial-temporal patterns and differences among
204 vegetation types. We collected $SIF_{\text{yield apparent}}$ of OCO-2 footprints for which the fraction of a
205 specific vegetation type is larger than 80%. For TROPOMI data, the threshold value of the
206 fraction was set to 50% for corn and soybean because few footprints remained when the

207 threshold value was set to 80%. The spatial patterns of $SIF_{\text{yield apparent}}$ of different vegetation
208 types for each month were smoothed by averaging all available $SIF_{\text{yield apparent}}$ of the specific
209 vegetation type within a $0.5^\circ \times 0.5^\circ$ grid. Seasonal patterns of $SIF_{\text{yield apparent}}$ were examined. The
210 study area was divided into three sub-regions for each vegetation type according to spatial
211 distributions of the footprints, and temporal dynamics of monthly mean $SIF_{\text{yield apparent}}$ were
212 plotted for the three sub-regions.

213 Variability of $SIF_{\text{yield apparent}}$ could be driven by several potential factors. First, we examined
214 impacts of air temperature and precipitation on $SIF_{\text{yield apparent}}$, because these climate variables
215 could affect $SIF_{\text{yield apparent}}$ through either f^{esc} or Φ_F . We plotted $SIF_{\text{yield apparent}}$ of each vegetation
216 type in each growing season month within a climate space built by a multi-year average of
217 monthly mean air temperature and monthly total precipitation. Mean air temperature and total
218 precipitation for May to September were calculated from monthly PRISM Climate data with a
219 spatial resolution of 4 km from 2015 to 2018 (<http://prism.oregonstate.edu/>, Daly et al., 2008).
220 Second, we examined differences in $SIF_{\text{yield apparent}}$ between grass and pasture, and among
221 different forest types which could also arise from f^{esc} and Φ_F . The USGS National Land Cover
222 Database (NLCD) in 2016 was used to identify grass (Grassland/Herbaceous in NLCD land
223 cover classification) and pasture (Pasture/Hay in NLCD land cover classification, Homer,
224 2015). Forest types were identified according to the Conus Forest Group dataset downloaded
225 from USDA Forest Service (https://data.fs.usda.gov/geodata/rastergateway/forest_type/). This
226 dataset is created by the USFS Forest Inventory and Analysis program and the Remote Sensing
227 Application Center. Third, the start of the growing season (SOS) of the four vegetation types
228 was examined based on the Normalized Difference Phenology Index (Wang et al., 2017, Text

229 S2). Finally, variabilities of f^{esc} and Φ_F can help explain the variabilities of $\text{SIF}_{\text{yield apparent}}$. We
230 examined the differences of f^{esc} and Φ_F between croplands and non-croplands, and between
231 corn and soybean. We also explored the spatial and temporal patterns of f^{esc} and Φ_F . The same
232 analysis as for $\text{SIF}_{\text{yield apparent}}$ was conducted.

233

234 **3. Results**

235 **3.1 Difference of $\text{SIF}_{\text{yield apparent}}$ between croplands and non-croplands**

236 The relationship between OCO-2 $\text{SIF}_{\text{yield apparent}}$ and cropland fraction in different growing
237 months from 2015 to 2018 (Fig. 3) showed a clear seasonal pattern. In May, $\text{SIF}_{\text{yield apparent}}$
238 decreased with the cropland fraction, implying that $\text{SIF}_{\text{yield apparent}}$ of croplands was lower than
239 non-croplands in the early growing season. In July and August, $\text{SIF}_{\text{yield apparent}}$ showed an
240 increasing trend with the increase of the cropland fraction (all statistically significant with
241 $P < 0.001$). These results indicated that during the peak growing season, cropland $\text{SIF}_{\text{yield apparent}}$
242 was higher than non-cropland $\text{SIF}_{\text{yield apparent}}$.

243 Since we have SIF footprint observations from TROPOMI in 2018, we applied the same
 244 analysis as above (Fig. S1). Generally, the results from TROPOMI observations were similar
 245 to those from OCO-2 observations, despite the different magnitudes of the slopes between
 246 $SIF_{\text{yield apparent}}$ and the cropland fraction. We further conducted the same analysis for SIF_{inst}
 247 (instantaneous SIF) and SIF_{par} (SIF normalized by PAR, Fig. S2). The difference between
 248 croplands and non-croplands in SIF_{inst} and SIF_{par} showed a similar seasonal pattern to that of
 249 $SIF_{\text{yield apparent}}$.

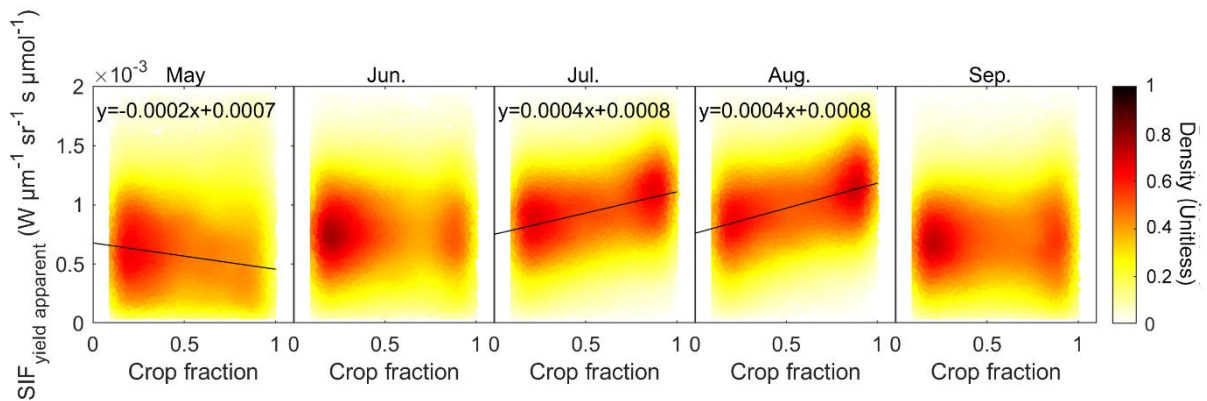


Fig. 3 Relationship between $SIF_{\text{yield apparent}}$ calculated from OCO-2 SIF and the fraction of croplands (corn and soybean). The linear fits and the equations are shown when the regression is significant ($p < 0.001$). Only footprints with a cropland fraction larger than 10% are included.

250
 251
 252

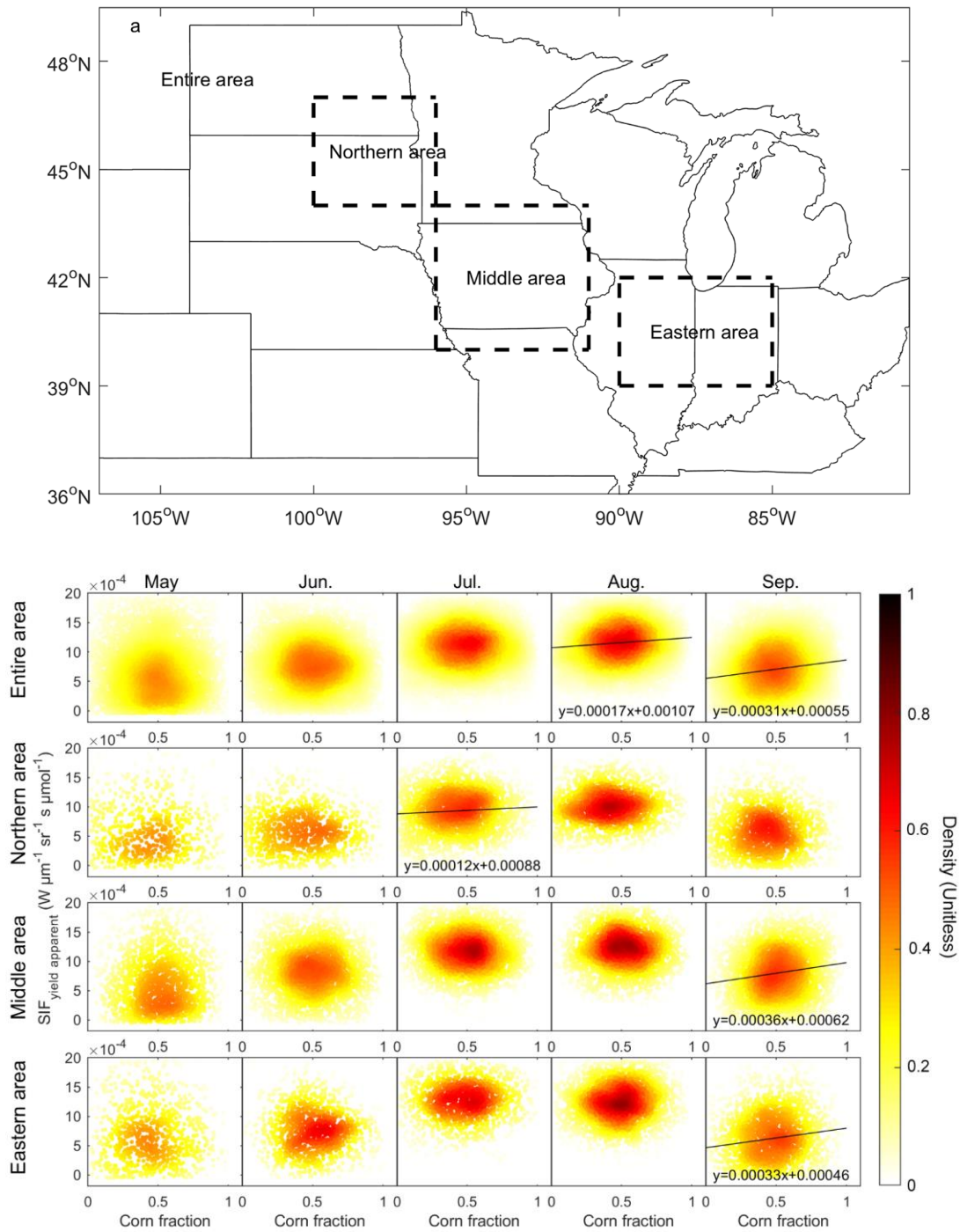


Fig. 4 Relationship between $SIF_{yield\ apparent}$ and the fraction of the OCO-2 footprint covered by corn. The upper panel illustrates the three regions that are labeled in the bottom panel. The linear fits and the equations in the bottom panel are shown only when the regression is significant ($p < 0.001$). Only footprints with a cropland fraction larger than 80% were included.

255 **3.2 Difference of $SIF_{\text{yield apparent}}$ between Corn (C4) and Soybean (C3)**

256 The relationship between OCO-2 $SIF_{\text{yield apparent}}$ and corn fraction for the cropland-
257 dominated footprints during different growing season months from 2015 to 2018 for different
258 regions (Fig. 4) generally showed a weak linear relationship between $SIF_{\text{yield apparent}}$ and corn
259 fraction, implying that $SIF_{\text{yield apparent}}$ of corn was similar to that of soybean. For the entire study
260 domain, the relationship between $SIF_{\text{yield apparent}}$ and corn fraction was positively significant
261 ($P < 0.001$) in August and September but was not significant in the other three months. We also
262 performed a linear regression between $SIF_{\text{yield apparent}}$ and corn fraction in three sub-regions
263 (northern area, middle area, and eastern area) and in five growing season months respectively,
264 with a total of 15 cases (Fig. 4). The relationship was significant ($P < 0.001$) only in three out of
265 the 15 cases: the northern area in July, the middle area in September, and the eastern area in
266 September. Compared with $SIF_{\text{yield apparent}}$, the difference of SIF_{inst} and SIF_{par} between corn and
267 soybean appeared to be similar (Fig. S3-S4). SIF_{inst} and SIF_{par} of corn were significantly larger
268 than soybean from June to September for the entire area. However, this difference was weak
269 when the analysis was restricted to a small sub-region, with the exception of SIF_{inst} in the
270 northern area.

271

272 **3.3 Spatial and temporal patterns of $SIF_{\text{yield apparent}}$**

273 **3.3.1 Spatial pattern and potential drivers of $SIF_{\text{yield apparent}}$**

274 $SIF_{\text{yield apparent}}$ of corn and soybean calculated from the OCO-2 footprint data showed clear
275 spatial patterns (Fig. 5). In May and June, the spatial difference of $SIF_{\text{yield apparent}}$ was low for

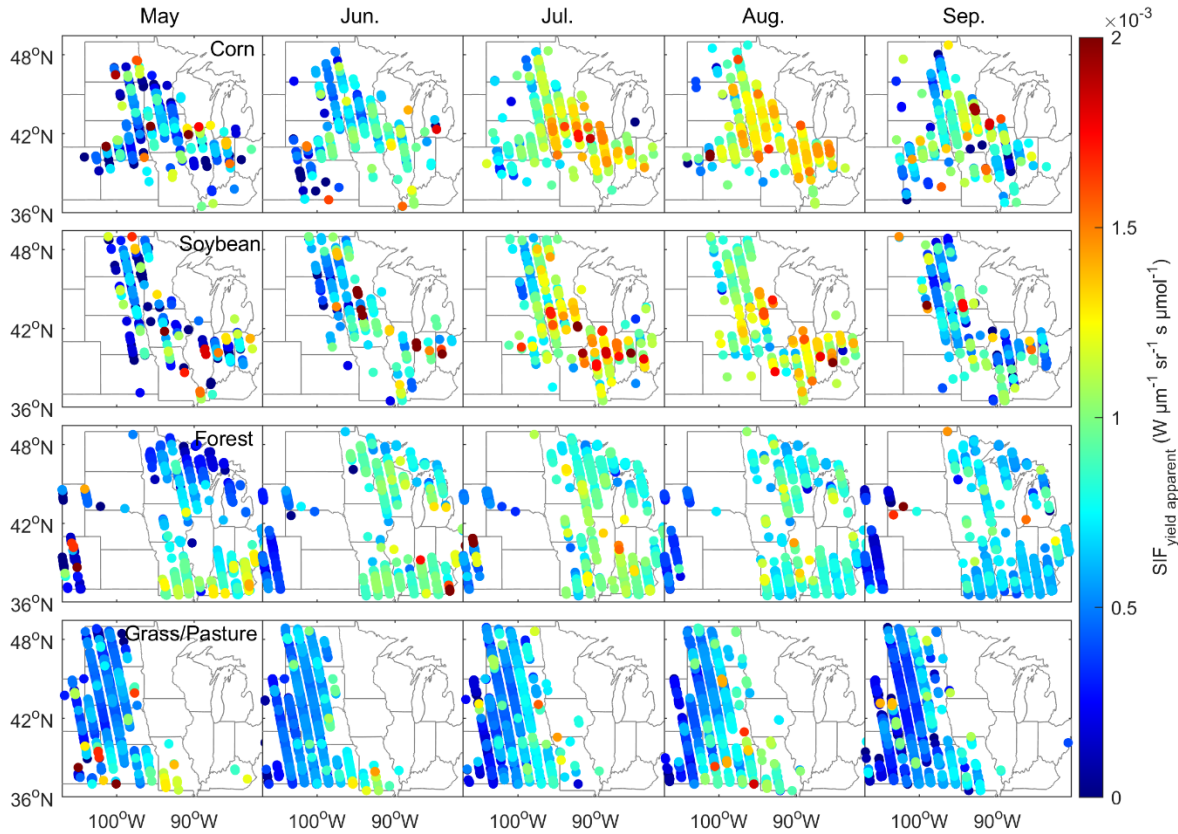


Fig. 5 Spatial distributions of $SIF_{\text{yield apparent}}$ of corn, soybean, forest, and grassland calculated from the OCO-2 data. The average of all the available $SIF_{\text{yield apparent}}$ values within a $0.5^\circ \times 0.5^\circ$ grid was assigned to all the footprints within the grid.

276 both corn and soybean because it is the beginning of the growing season for those crops (Fig.
 277 S5). From July to August, $SIF_{\text{yield apparent}}$ of corn in the central Corn Belt (Iowa, Illinois, and
 278 Indiana) was higher than $SIF_{\text{yield apparent}}$ of corn in the northern and the western parts of the Corn
 279 Belt. $SIF_{\text{yield apparent}}$ of soybean showed a similar pattern to corn, despite there were fewer
 280 available observations defined as the fraction of soybean >80% of the footprint in the west.

281 This spatial pattern of $SIF_{\text{yield apparent}}$ for both corn and soybean can be partly explained by
 282 precipitation (Fig. 6). During the peak growing season, $SIF_{\text{yield apparent}}$ was, in general, higher in
 283 areas with higher precipitation. $SIF_{\text{yield apparent}}$ in July was significantly ($P < 0.01$) correlated with
 284 precipitation when the temperature was fixed to a small range. The response of $SIF_{\text{yield apparent}}$ to

285 temperature was not clear. The linear correlation between $SIF_{\text{yield apparent}}$ in July and temperature
286 was not significant when precipitation was fixed to a small range. In September, except for a
287 small region in the central Corn Belt with high values of $SIF_{\text{yield apparent}}$ of corn, $SIF_{\text{yield apparent}}$ of
288 the two crop types started to decrease, possibly because both crops matured.

289 Spatial patterns of $SIF_{\text{yield apparent}}$ of forest and grass/pasture differed from those of corn and
290 soybean (Fig. 5). In general, Forest $SIF_{\text{yield apparent}}$ in the west was much lower than in other
291 regions during the growing season. Forest $SIF_{\text{yield apparent}}$ in the northeast and southeast were
292 comparable. Two factors could potentially account for the observed spatial patterns. First, high
293 $SIF_{\text{yield apparent}}$ was associated with high temperature and precipitation (Fig. 6). Second, the
294 spatial distribution of the forest types and the differences of $SIF_{\text{yield apparent}}$ among these types
295 could explained the spatial pattern of $SIF_{\text{yield apparent}}$. Among all forest types, $SIF_{\text{yield apparent}}$ of the
296 dominant forest type in the west (Ponderosa Pine) was the lowest, and $SIF_{\text{yield apparent}}$ of the
297 dominant forest type in the southeast (Oak/Hickory) was the highest (Fig. 7). In addition to the
298 general spatial pattern, a decreasing pattern of $SIF_{\text{yield apparent}}$ from the southeast to the northeast
299 was observed in May. A potential explanation for this observation is that the SOS of forest in
300 the northeast was in early May or late April, whereas the SOS of forest in the southeast was in
301 March or April (Fig. S5).

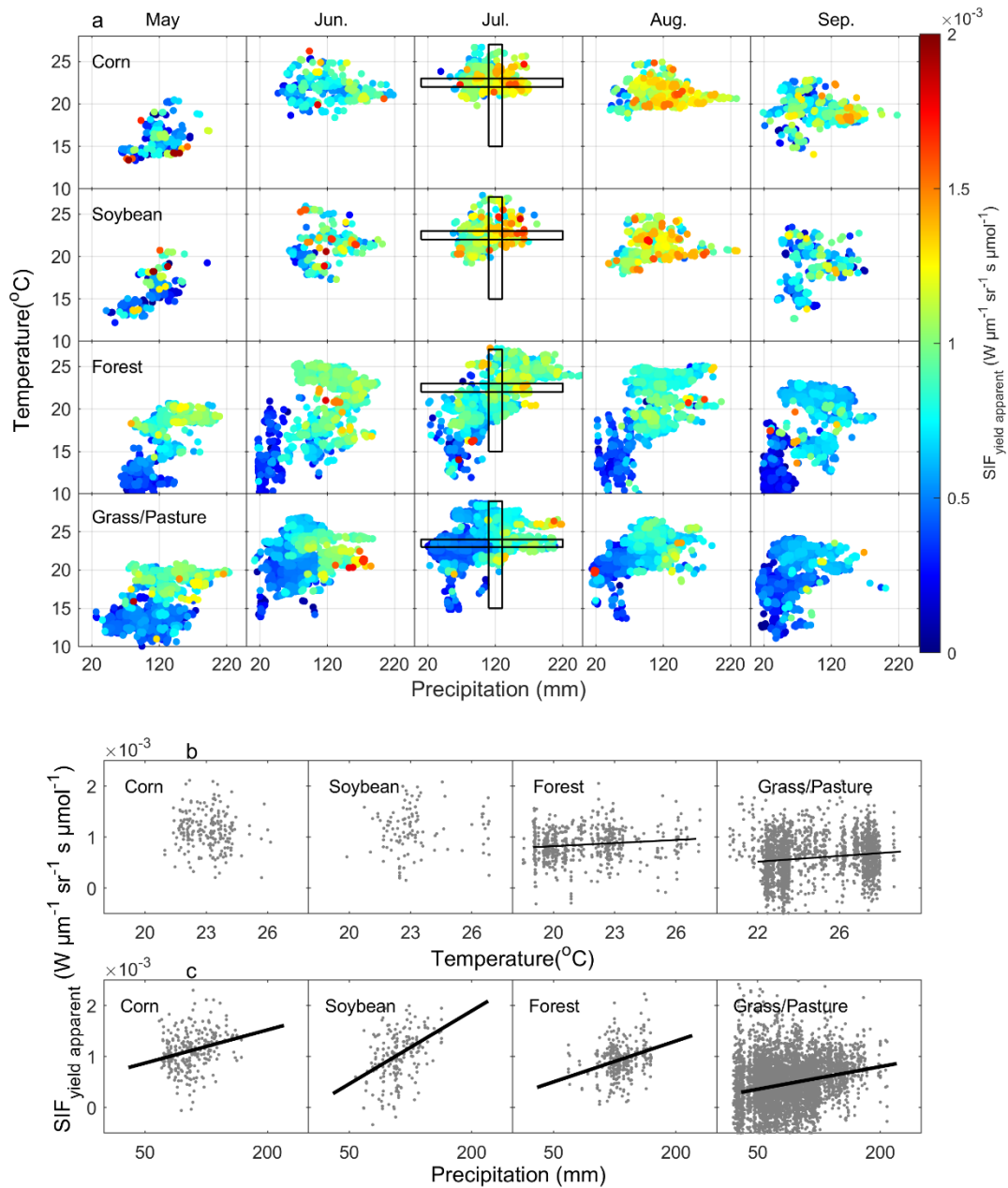


Fig. 6 a, Distributions of $SIF_{\text{yield apparent}}$ of corn, soybean, forest, and grass/pasture within a 2-D space jointly determined by monthly mean temperature ($^{\circ}\text{C}$) and precipitation (mm). The $SIF_{\text{yield apparent}}$ was calculated from the OCO-2 footprint data from 2015 to 2018. The meteorological variables are multi-year mean values. $SIF_{\text{yield apparent}}$ was smoothed by averaging SIF_{yield} within a $10\text{ mm} \times 0.5\text{ }^{\circ}\text{C}$ window. b, Scatter plots of $SIF_{\text{yield apparent}}$ versus mean temperature used data in the vertical box shown in a. c, Scatter plots of $SIF_{\text{yield apparent}}$ versus total precipitation used data in the horizontal box shown in a. The linear fits are shown only when the regression is significant ($p < 0.01$).

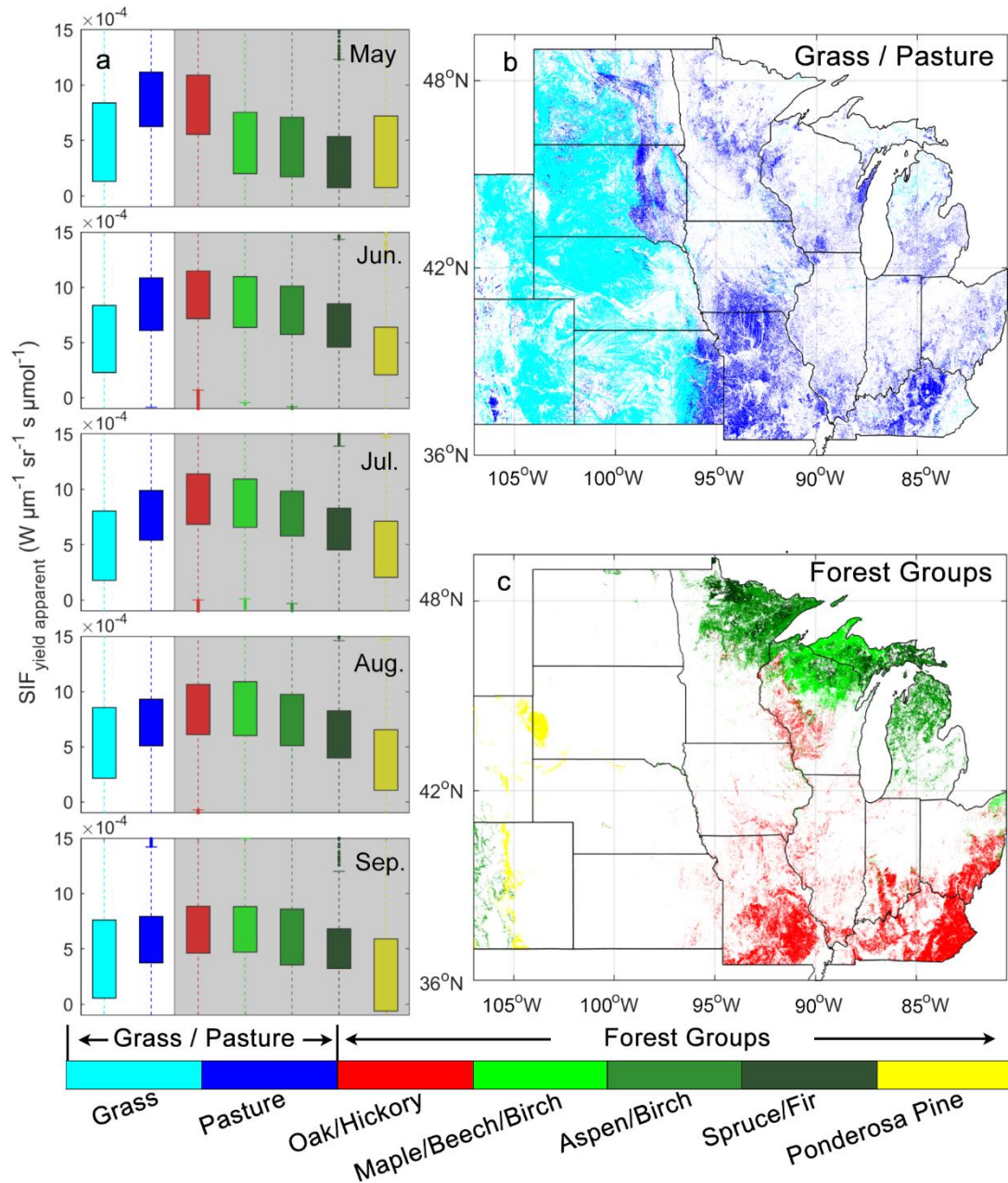


Fig. 7 Boxplots of $SIF_{yield\ apparent}$ of grass, pasture and different forest types for different months. Shaded areas are forest types. $SIF_{yield\ apparent}$ was calculated from OCO-2 footprint data from 2015 to 2018.

303

304 The spatial pattern of $SIF_{yield\ apparent}$ in grass/pasture demonstrated a clear gradient of

305 increase from west to east. This pattern was consistent across different growing months.

306 Grass/pasture is mainly distributed in the western part of the U.S. Midwest. $SIF_{\text{yield apparent}}$ of
307 grass/pasture appeared to be lower than other vegetation types, which may also contribute to a
308 lower spatial variability. Similar to the forest, the spatial variability could potentially be
309 explained by two factors. First, $SIF_{\text{yield apparent}}$ of pasture was higher than that of grassland while
310 pasture was mainly distributed in the east and grassland was distributed in the west. However,
311 this may only account for a small portion of the spatial pattern of $SIF_{\text{yield apparent}}$, because the
312 number of footprints in pasture areas was limited. Second, high $SIF_{\text{yield apparent}}$ was observed in
313 the wet-warm region (Fig. 6), implying the impact of meteorological factors on $SIF_{\text{yield apparent}}$.
314 $SIF_{\text{yield apparent}}$ in July was positively correlated with temperature (or precipitation) after fixing
315 precipitation (or temperature, Fig. 6).

316 To further corroborate our findings, we examined the spatial pattern of $SIF_{\text{yield apparent}}$ for
317 the four vegetation types in 2018 using TROPOMI footprint data, as Fig. S6. Compared with
318 the results from OCO-2, the spatial pattern of $SIF_{\text{yield apparent}}$ of corn from TROPOMI showed
319 high values in eastern Nebraska, southern Iowa, and Illinois in June. For soybean, $SIF_{\text{yield apparent}}$
320 was high in the southern region. Despite these slight differences, results from the two datasets
321 were similar. We also explored spatial patterns of SIF_{par} and SIF_{inst} and found similar spatial
322 patterns to $SIF_{\text{yield apparent}}$ (Fig. S7-S8).

323 **3.3.2 Temporal (Seasonal) pattern of $SIF_{\text{yield apparent}}$**

324 $SIF_{\text{yield apparent}}$ of corn, soybean, grass/pasture, and forest had different temporal variabilities
325 from May to September (Fig. 8). Seasonal patterns of $SIF_{\text{yield apparent}}$ of corn and soybean showed
326 a ‘bell’ shape. $SIF_{\text{yield apparent}}$ of corn and soybean increased from May onward, reaching the

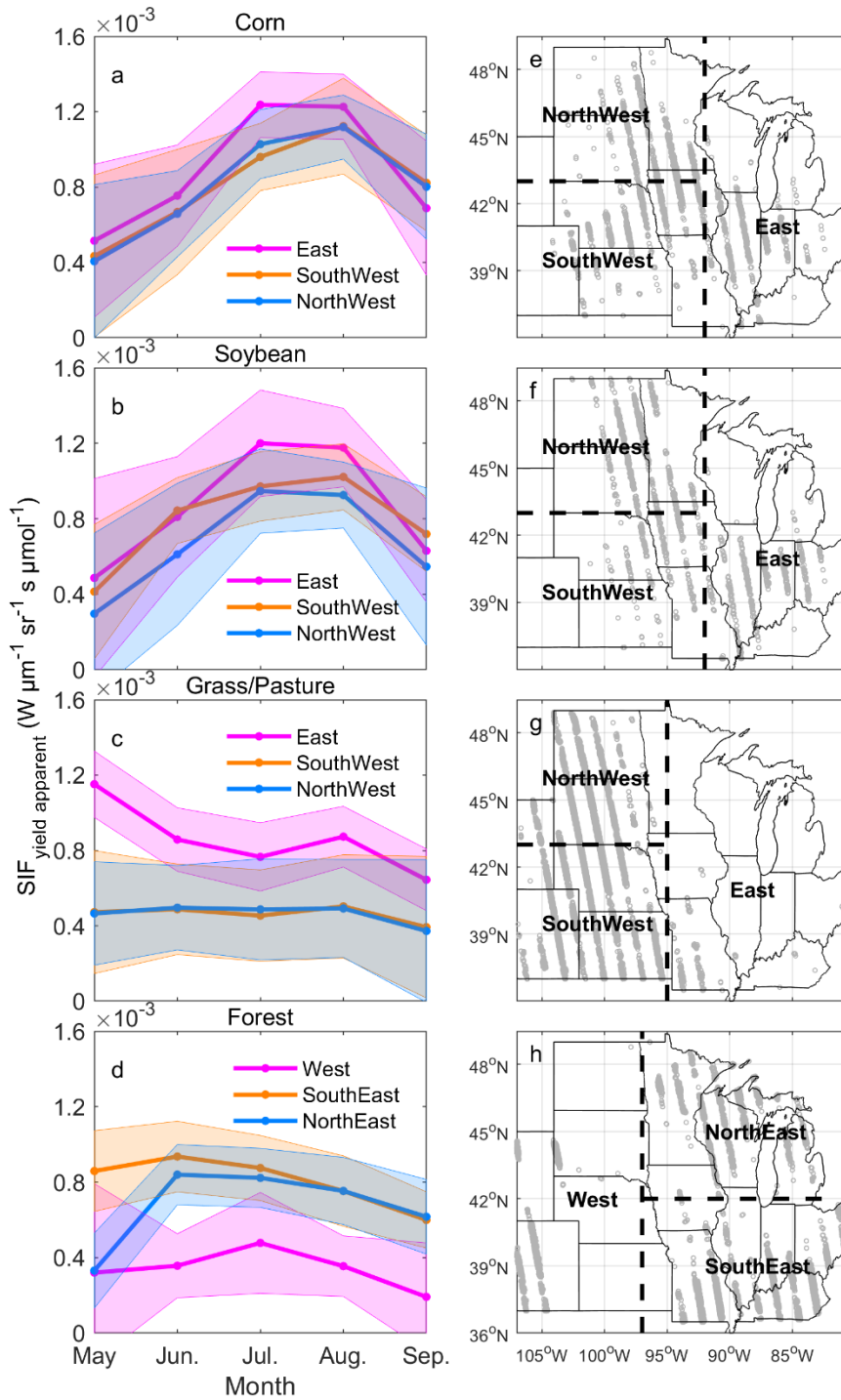


Fig. 8 Seasonal patterns of SIF_{yield apparent} of corn, soybean, forest, and grassland in different regions, from OCO-2 footprint data (a-d). Each line was calculated as the median value of all footprints and all years within a specific region. Shading indicates one standard deviation. e-h show the definitions of the different regions in a-d.

327 highest values in July or August, before decreasing to a lower value in September when crops

328 began to senesce. Despite differences in the magnitude of $SIF_{\text{yield apparent}}$, this seasonal pattern
329 was consistent across different sub-regions.

330 For grass/pasture, the seasonal pattern of $SIF_{\text{yield apparent}}$ in the west was remarkably
331 different from that in the east (Fig. 8). $SIF_{\text{yield apparent}}$ in the west showed a slightly decreasing
332 trend from May to September, while in the east, $SIF_{\text{yield apparent}}$ decreased from May to September
333 with a higher magnitude of $SIF_{\text{yield apparent}}$ during the growing season. Notably, there was a rapid
334 decrease in $SIF_{\text{yield apparent}}$ from May to June. This may indicate that the seasonal pattern of
335 $SIF_{\text{yield apparent}}$ of grass, which dominates in the west, differs from that of pasture, which
336 dominates in the east (Fig. 7).

337 For forest distributed in different sub-regions, there was a lack of a universal temporal
338 pattern, possibly due to the different dominant forest types in these sub-regions (Fig. 7). In the
339 west, $SIF_{\text{yield apparent}}$ of forest started increasing in May, peaked in July and then decreased until
340 September. In the southeast, $SIF_{\text{yield apparent}}$ showed a decreasing trend from May to September.
341 In the northeast, $SIF_{\text{yield apparent}}$ of the forest showed a very large increase from May to June.
342 possibly because the growing season of the forests in this area starts in May after which time
343 $SIF_{\text{yield apparent}}$ decreases until September.

344 We further examined seasonal patterns of $SIF_{\text{yield apparent}}$ derived from TROPOMI in 2018
345 (Fig S9.). As expected, the monthly dynamics of $SIF_{\text{yield apparent}}$ from May to September derived
346 from the two satellite observations were similar, except for grass/pasture in the east where
347 $SIF_{\text{yield apparent}}$ from TROPOMI did not show a clear decreasing trend from May to September
348 as OCO-2. In addition, the seasonal patterns of SIF_{par} and SIF_{inst} were similar to those of SIF_{yield}
349 apparent (Fig. S10-S11).

350

351 **3.4 Variability of f^{esc} and Φ_F**

352 The density plots showing the relationships between Φ_F or f^{esc} and croplands fraction (Fig.
353 S12) suggested that both Φ_F and f^{esc} contributed to the observed difference of $\text{SIF}_{\text{yield apparent}}$
354 between croplands and non-croplands. f^{esc} had a strong linear relationship with crop fraction
355 during different growing months, while the relationship between Φ_F and crop fraction was
356 relatively weak compared with the relationship between f^{esc} and crop fraction. The seasonal
357 dynamics of the slope between f^{esc} and crop fraction were similar to those observed between
358 $\text{SIF}_{\text{yield apparent}}$ and crop fraction. These results imply that f^{esc} may dominate the observed
359 differences in $\text{SIF}_{\text{yield apparent}}$ between croplands and non-croplands.

360 Differences of Φ_F or f^{esc} between corn and soybean can be detected during some months
361 (Fig. S13-S14), although $\text{SIF}_{\text{yield apparent}}$ of corn and soybean were not significantly different
362 across the three sub-regions (Fig 5). For example, in August, the Φ_F of corn was larger than that
363 of soybean, while the f^{esc} of corn was smaller than that of soybean in the three sub-regions or
364 over the whole study domain. In September, corn f^{esc} was significantly lower than soybean f^{esc}
365 while the Φ_F of corn was larger than that of soybean in the east and middle sub-regions or over
366 the whole domain.

367 Fig. S15 and Fig S16 showed spatial patterns of f^{esc} and Φ_F . The spatial pattern of f^{esc} was
368 similar to that of $\text{SIF}_{\text{yield apparent}}$. On the other hand, the spatial pattern of Φ_F contained more noise.
369 No clear spatial pattern was found except that Φ_F of grass/pasture increased from the west to
370 the east, which matched with the pattern of $\text{SIF}_{\text{yield apparent}}$. Fig. 9 showed the seasonal patterns
371 of Φ_F and f^{esc} . Φ_F generally remained stable during the growing season for all the four vegetation

372 types except for the increase from May to June for croplands. Conversely, f^{esc} showed a strong
373 seasonal variability which was similar to that of $\text{SIF}_{\text{yield}}$ apparent.

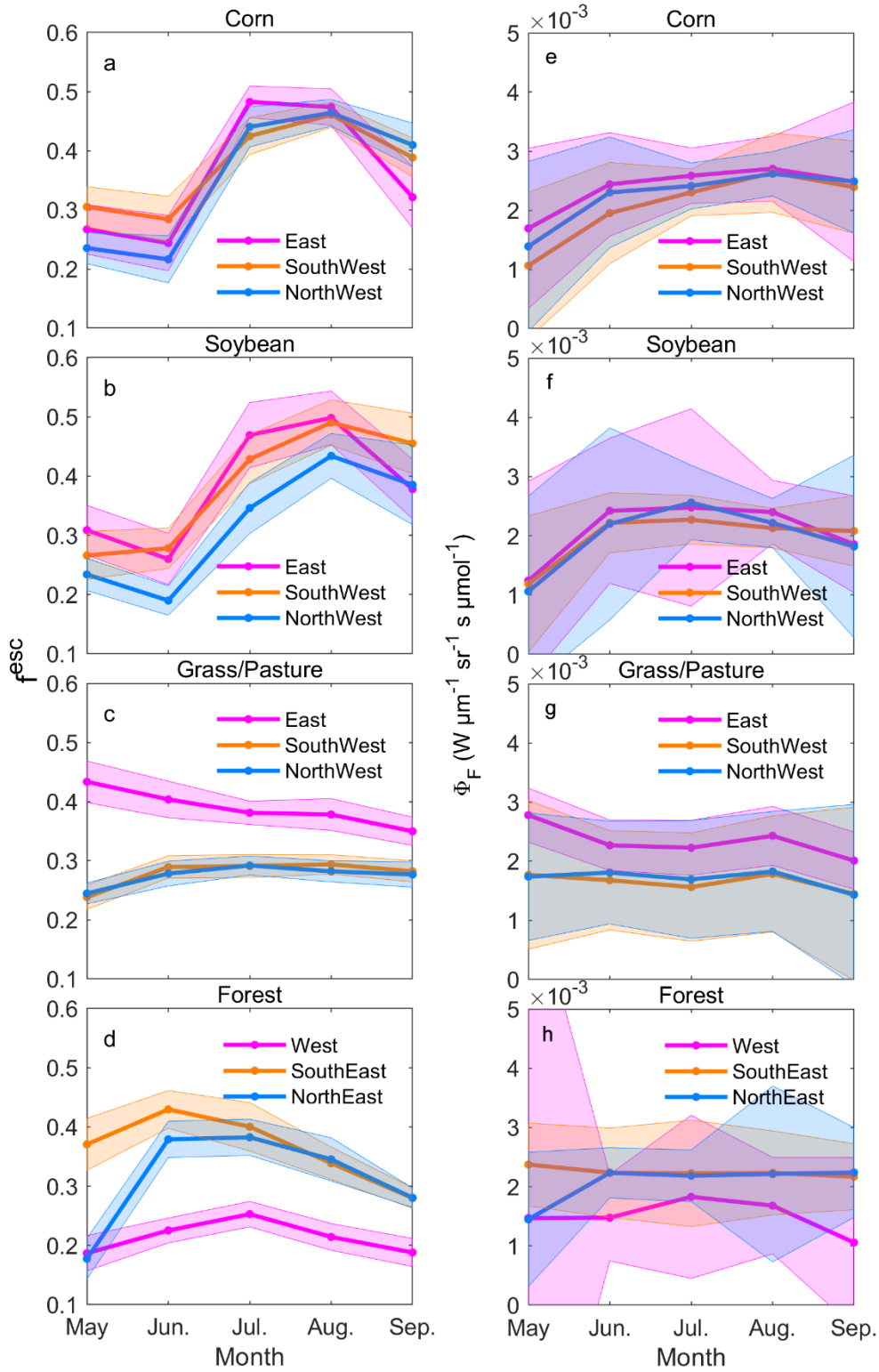


Fig. 9 Seasonal patterns of Φ_F and f^{esc} of corn, soybean, forest, and grassland in different regions from OCO-2 footprint data. Each line was calculated as the median value of all footprints the regions defined in Fig. 8. Shading indicates one standard deviation.

375 **4. Discussion**

376 **4.1 Variability of $SIF_{\text{yield apparent}}$**

377 Our study shows that $SIF_{\text{yield apparent}}$ of croplands is significantly larger than non-croplands
378 during the peak growing season in the U.S. Midwest (July-August). This result is consistent
379 with the spatial pattern of SIF during the same period in the U.S. Midwest observed in previous
380 research which reveals much higher SIF values in the Corn Belt than in the surrounding regions
381 (Guanter et al., 2014; Gentine and Alemohammad 2018; Joiner et al., 2013). The higher SIF of
382 croplands compared with non-croplands is also supported by the OCO-2 footprint SIF data used
383 in this study (Fig. S3). Our analysis of $SIF_{\text{yield apparent}}$ demonstrates that the differences in SIF_{yield}
384 apparent between croplands and non-croplands could partly contribute to the remarkably high SIF
385 of the U.S. Corn Belt. APAR also contributes to the high SIF (Fig. S17) but is less important
386 than $SIF_{\text{yield apparent}}$. Because the ratio of croplands $SIF_{\text{yield apparent}}$ to non-croplands $SIF_{\text{yield apparent}}$
387 in peak season, which can be roughly estimated from equations in Fig. 3 when crop fraction is
388 set as 1 and 0, is much higher than that of APAR (Fig. S17).

389 The difference in $SIF_{\text{yield apparent}}$ between the C4 (corn) and C3 (soybean) crops is small
390 (Fig. 4). In August and September, the Φ_F of corn is larger than soybean, while the f^{esc} of corn
391 shows the opposite patterns which potentially explain the similar $SIF_{\text{yield apparent}}$ of corn and
392 soybean in the two months (Fig. S13 and S14). For some other months, the similarities in f^{esc}
393 could possibly explain the similar patterns in $SIF_{\text{yield apparent}}$ given the small variation and
394 differences in Φ_F . Wood et al., (2017) examined OCO-2 footprint SIF retrievals in Iowa and
395 southern Minnesota and found a similar magnitude of fluorescence (F_s , SIF normalized by the
396 cosine of the solar zenith angle) from corn and soybean canopies. It is noteworthy that we also

397 do not find any significant difference in SIF_{par} (SIF normalized by PAR) between corn and
398 soybean in a similar region (middle area in Fig. 5). Here SIF_{par} is a similar concept to F_s because
399 the cosine of the solar zenith angle is a good proxy of PAR. However, when we focus on the
400 whole Midwest region, both SIF_{inst} and SIF_{par} of corn are larger than the counterparts of soybean
401 during the peak season probably because of the different spatial distribution between corn and
402 soybean.

403 We present different spatial patterns of $SIF_{yield\ apparent}$ of different vegetation types using
404 satellite footprint data. Previous studies have investigated spatial patterns of $SIF_{yield\ apparent}$ at
405 regional or global scales (Joiner et al., 2011; Li et al., 2018b; Song et al., 2018) using coarse-
406 spatial-resolution SIF products. Our study confirms that meteorological variables (e.g.
407 precipitation and temperature) play roles in determining $SIF_{yield\ apparent}$ within certain vegetation
408 types. In general, more precipitation leads to higher $SIF_{yield\ apparent}$ for all the vegetation types,
409 while the correlation between temperature and $SIF_{yield\ apparent}$ is weak. Considering that some
410 croplands are irrigated and precipitation might not directly affect the observed SIF, we checked
411 the impact of VPD (Fig. S18) on $SIF_{yield\ apparent}$ and found negative correlations between VPD
412 and $SIF_{yield\ apparent}$ for most cases.

413 The seasonal patterns of corn and soybean $SIF_{yield\ apparent}$ from May to September generally
414 follow the growth cycle of crops in the U.S. Midwest. The ‘bell’ shape curve was also found
415 for wheat in northwest India and crops in western Russia during the growing season, based on
416 the GOME-2 gridded dataset (Song et al., 2018; Yoshida et al., 2015). However, we did not
417 observe this bell shape of $SIF_{yield\ apparent}$ for forest and grass/pasture ecosystems, which is a
418 departure from prior studies (Yoshida et al., 2015). By extending the growing season to include

419 April and October, we found that $SIF_{\text{yield apparent}}$ of forest and grass/pasture increased during the
420 start of the growing season except for grass in the west and decreased during the end of the
421 growing season, although the amplitude of the shift of $SIF_{\text{yield apparent}}$ was not large (Fig. S19).
422 To confirm the results from satellite data, we also checked the seasonal pattern of $SIF_{\text{yield apparent}}$
423 using ground observations at two sites at Nebraska (Text S3). Fig. S20 showed that there was
424 a decreasing trend of $SIF_{\text{yield apparent}}$ from peak season to September for corn in 2017 and soybean
425 in 2018 which is consistent with the satellite observation. Currently, we cannot provide a more
426 detailed comparison because the ground data only cover the second half of the growing season
427 and there are not enough OCO-2 footprints that cover the field sites. The factors that we
428 observed to correlate with the spatial pattern of $SIF_{\text{yield apparent}}$, such as precipitation and
429 temperature, may influence the seasonal cycle of $SIF_{\text{yield apparent}}$ (Li et al., 2018b). We also
430 recognize that the seasonal cycle of plant growth usually resembles the seasonal cycle of
431 environmental factors, which makes it difficult to fully disentangle the influences of abiotic
432 factors (environmental factors) and physical factors (e.g. canopy structure, leaf optical property)
433 on $SIF_{\text{yield apparent}}$.

434

435 **4.2 Variabilities of f^{esc} and Φ_F**

436 The apparent canopy SIF yield is a product of f^{esc} and Φ_F . Our results suggest that f^{esc} may
437 be a major driver of the observed seasonal dynamic of $SIF_{\text{yield apparent}}$. The seasonal pattern of
438 f^{esc} is similar to that of $SIF_{\text{yield apparent}}$ for all the four vegetation types. We also notice that some
439 results are not as expected. For example, the seasonal pattern of f^{esc} of crops shows a large
440 increase from June to July. At first sight, we might expect that f^{esc} should decrease with the

441 rapid increase of LAI during the early growing season because the fraction of canopy gaps for
442 SIF to escape will decrease. However, for far-red SIF, previous studies based on the Soil
443 Canopy Observation, Photochemistry and Energy (SCOPE) model reported a contrary result
444 (Fournier et al., 2012; Du et al., 2017; Yang and Van der Tol, 2018). Escaping ratio increases
445 with LAI due to multiple scattering. LAD can also influence f^{esc} . Some simulation analyses
446 show that escaping ratio with planophile or spherical LAD is much higher than that of
447 erectophile vegetation (Migliavacca et al., 2017; Zeng et al., 2019), and experimental data also
448 support this argument (Du et al., 2017). However, more field observations are needed to address
449 whether there is a shift of erectophile canopy to planophile canopy for crops during the early
450 season. Another possible cause of the observed pattern is the increasing canopy cover in spring
451 in driving the increasing f^{esc} estimation. LAI and LAD could also be used to explain the low
452 value of f^{esc} of grassland in the west because the grass in arid and semi-arid regions usually has
453 low LAI and erectophile LAD (Diana et al., 2000; Holder et al., 2012). Compared to f^{esc} , the
454 monthly median value of Φ_F remains stable. However, the high variance of Φ_F within a month
455 implies that Φ_F may play an important role at small time scales. With regard to the spatial
456 pattern, we find a clear spatial pattern of f^{esc} , while the spatial pattern of Φ_F has more noise. A
457 probable explanation is that f^{esc} is determined by the canopy structure and leaf optical properties,
458 which are stable during specific time periods, whereas Φ_F reflects the physiology of vegetation
459 which can be influenced by more rapidly varying environmental conditions. Another simple
460 explanation is that the estimation of SIF contains more noise than the estimation of f^{esc} .

461 The impact of meteorological factors on $\text{SIF}_{\text{yield apparent}}$ could be attributable at least in part
462 to both f^{esc} and Φ_F . The spatial pattern of f^{esc} can be influenced by meteorological factors. For

463 example, the LAD of soybeans is controlled by leaf water potential, and under water stress
464 conditions, soybean leaves tend to be more vertical (Oosterhuis et al., 1985). Additionally,
465 plants in arid areas may have steeper leaf angles to reduce rainfall interception by leaves and
466 increase soil infiltration (Holder, 2012) or to minimize light interception and leaf temperature
467 which is usually in excess in those regions. Similarly, LAI of grass has been reported to increase
468 with precipitation (Diana et al., 2000), which could also change f^{esc} . Φ_F reflects the distribution
469 of the absorbed energy, which is likely also sensitive to meteorological conditions through the
470 dynamics changes of non-photochemical quenching (NPQ) and photochemical quenching (PQ)
471 in relation to various plant abiotic stresses (Cendrero-mateo et al., 2015; Frankenberg and Berry,
472 2018; Xu et al., 2018).

473 **4.3 Uncertainties and Limitations**

474 Quantifying f^{esc} and Φ_F over large scales is a challenging but important task. A handful of
475 methods have been developed (Liu et al., 2018; Romero et al., 2018; Yang and van der Tol,
476 2018; Zeng et al., 2019). We adopt a method developed recently by Zeng et al. (2019), which
477 can be easily applied over large spatial scales. The approach is demonstrated to be effective by
478 simulation analysis using the SCOPE model and the Discrete Anisotropic Radiative Transfer
479 (DART) model. But some uncertainties are introduced during the application of the approach.
480 First, wavelengths of SIF (771nm and 757 nm for OCO-2, 740 nm for TROPOMI) are not
481 consistent with the MODIS NIR band (858 nm) which is used to calculate f^{esc} . However, this
482 impact is small in practice, as assessed by Zeng et al., (2019). Second, the sun-canopy-sensor
483 geometry of SIF is different from that of MODIS. To minimize this effect, we only used OCO-
484 2 observations taken in ‘nadir’ mode, TROPOMI data with view zenith angle less than 10

485 degrees, and MODIS Nadir BRDF-Adjusted Reflectance data. The uncertainty caused by sun-
486 canopy-sensor geometry could also influence the seasonal pattern of $SIF_{\text{yield apparent}}$ due to the
487 varying solar zenith angle for different seasons. Third, when vegetation cover is extremely low,
488 this approach can break down (Zeng et al., 2019). Although there are some potential
489 uncertainties in the analysis, it is an important step toward decomposing $SIF_{\text{yield apparent}}$ into f^{esc}
490 and Φ_F , which represents a necessary advancement toward fully interpreting observed SIF
491 signals.

492 Accurate estimation of $SIF_{\text{yield apparent}}$ depends on reliable fPAR datasets. There are several
493 fPAR products available. These datasets are produced from measurements from different
494 instruments using different retrieval algorithms which potentially generate discrepancies
495 among fPAR datasets. For example, inter-comparisons with other fPAR products show that
496 there is an overestimation of the retrievals at low fPAR values in MODIS fPAR products (Yan
497 et al., 2016). In this study, we used four approaches to estimate fPAR. Fig. S21 showed the
498 standard deviation (SD) of $SIF_{\text{yield apparent}}$ calculated from the four fPAR values. The results
499 demonstrated that the SD was much lower than the corresponding mean $SIF_{\text{yield apparent}}$ (Fig. 5)
500 for most cases, while for corn and soybean in May, the SD could be higher. This is probably
501 because the relative uncertainties of all terms in $SIF_{\text{yield apparent}}$ and f^{esc} are higher for low fPAR
502 values.

503 Although this study used state-of-the-art satellite-based SIF products, these SIF products
504 still have limitations. First, SIF is a weak signal consisting of 1%-5% of the total absorbed
505 energy (Frankenberg et al., 2018), and satellite-based SIF measurements still contain possibly
506 uncertainties. Sun et al., (2017) compared OCO-2 retrievals with airborne measurements of SIF

507 with the Chlorophyll Fluorescence Imaging Spectrometer (CFIS) and found R^2 between OCO-
508 2 and CFIS SIF was 0.71. Second, OCO-2 footprint observations are discrete samples, and they
509 are not spatially and temporally continuous. We also used TROPOMI footprint data which
510 provides better spatial and temporal details due to the greatly improved spatio-temporal
511 coverage of the dataset compared with OCO-2. However, we found some areas with lower valid
512 data coverage, for example, soybean crops in Iowa. This is probably because the spatial
513 resolution of TROPOMI is not fine enough to get enough pure footprints. The readers should
514 be aware that there is a consistent difference in the absolute value of SIF between OCO-2 and
515 TROPOMI because the wavelength of the two SIF retrievals is not the same. An alternative
516 method would be to use downscaled (Duveiller and Cescatti, 2016) or reconstructed (Gentine
517 and Alemohammad, 2018; Li and Xiao, 2019; Y. Zhang et al., 2018) gridded SIF data. However,
518 we purposely decided not to use any of these SIF products here, as these downscaled or
519 reconstructed data include assumptions that could skew our findings. Third, the temporal
520 frequency (monthly) in our analysis offers only a coarse view of seasonal patterns. Especially
521 during the period from May to June for crops and forests in the northeast when the plants start
522 to grow and the canopy structures and physiology status change rapidly. This could potentially
523 be solved with TROPOMI data with high temporal frequency in the future. New measurements
524 from the site level scale could provide more information. Finally, $SIF_{\text{yield apparent}}$ should be
525 wavelength dependent since both the emitted SIF spectrum and the reflectance at leaf level are
526 wavelength-dependent (Verrelst et al., 2015). However, the OCO-2 footprint dataset provides
527 SIF at 771 nm and 757 nm, while TROPOMI SIF is only available at 740 nm.

528 **4.4 Contribution to understand SIF and the $SIF_{\text{yield apparent}}$: LUE relationship**

529 This study's findings have many important implications. Most importantly, APAR and
530 $SIF_{\text{yield apparent}}$ jointly determine variability in SIF. APAR correlates more with plant structural
531 properties and pigment content, while $SIF_{\text{yield apparent}}$ is likely to carry both canopy structure and
532 plant physiology signals. Leaf-level and canopy-level studies have found evidence of potential
533 effects from plant physiological such as V_{cmax} etc. (Zhang et al., 2014), stomatal conductance
534 (Flexas et al., 2002), and electron transport rate (Guan et al., 2016), as well as canopy structure
535 (Fournier et al., 2012) such as LAD (Du et al., 2017; Zhang et al., 2016) and LAI (Du et al.,
536 2017; Yang and van der Tol, 2018). Our regional-level study reveals differences in SIF_{yield}
537 apparent across space and time and between vegetation cover types implying the importance of
538 $SIF_{\text{yield apparent}}$ in driving the variability of canopy SIF. The findings further emphasize the
539 important role of the escaping ratio (canopy structure).

540 The significant variations of $SIF_{\text{yield apparent}}$ revealed in this study may help foster modeling
541 of GPP at large scales. Similarities between the GPP and SIF equations (Equation 1 and 2) lead
542 to a formal equivalence between GPP: SIF and LUE: $SIF_{\text{yield apparent}}$. The equivalence of the two
543 equations could help to estimate GPP directly from satellite SIF observation and to better
544 understand what determines the GPP: SIF slope but only when a mechanistic relationship
545 between LUE and $SIF_{\text{yield apparent}}$ is established. Physiologically, there is a complicated coupling
546 between LUE and Φ_F under various light and plant stress conditions (Schlau-Cohen and Berry
547 2015, Van Der Tol et al., 2014). In addition to Φ_F , f^{esc} and LUE may also casually covary due to
548 temporal covariation between plant structure and plant function. The near-infrared reflectance
549 is related to leaf nitrogen content and the ratio of sun-exposed leaf area to total leaf area which
550 are determinants of photosynthetic capacity (Ollinger et al., 2008, Knyazikhin et al., 2013).

551 Meanwhile, the near-infrared reflectance is also supposed to be correlated to f^{esc} (Yang and van
552 der Tol, 2018). Thus the variability of f^{esc} may be associated with the variability of LUE. Studies
553 using field-level observations have intended to provide an empirical estimation of the LUE:
554 $\text{SIF}_{\text{yield apparent}}$ relationship (Damm et al., 2010; Miao et al., 2018; Verma et al., 2017; Yang et
555 al., 2018; Yang et al., 2015). However, the relationship varies across different seasons and
556 environmental conditions. Further efforts are required by combining field-level observations,
557 especially long-term observations (Miao et al., 2018; Yang et al., 2018), and satellite
558 observations to constrain these relationships and advance understanding of the underlying
559 controlling factors.

560

561 **5. Conclusions**

562 In this study, we conducted a systematic assessment of the spatio-temporal variability of
563 $\text{SIF}_{\text{yield apparent}}$ of corn, soybean, forest, and grass/pasture in the U.S. Midwest during the crop
564 growing season. The state-of-the-art satellite-based SIF products from OCO-2 and TROPOMI
565 footprint retrievals were used to estimate $\text{SIF}_{\text{yield apparent}}$ of specific vegetation types. The high
566 spatial resolution of the footprints enables accurate estimation of $\text{SIF}_{\text{yield apparent}}$ for each
567 vegetation type by reducing the intra-pixel mixture effects. Our analysis leads to four main
568 conclusions: 1) $\text{SIF}_{\text{yield apparent}}$ of croplands (i.e. corn and soybean) was higher than that of non-
569 croplands during the peak growing season (July and August) which contributed to the high SIF
570 observed in the U.S. Corn Belt in the summer. 2) $\text{SIF}_{\text{yield apparent}}$ of corn and soybean did not
571 show significant differences. 3) Different seasonal and spatial patterns of $\text{SIF}_{\text{yield apparent}}$ were
572 observed among the four vegetation types, which can be partially explained by meteorological

573 factors (i.e. precipitation and temperature) and intra-vegetation type variability (i.e. among
574 different forest types, and between grass and pasture). 4) The escaping ratio may be the major
575 driver of the observed variability of $SIF_{\text{yield apparent}}$.

576

577 **Acknowledgments:**

578 K.G., C.W., J.C., B.P., C.A., G.M., thank the financial support from NASA Terrestrial
579 Ecosystem Program through the Carbon Monitoring System Program (80NSSC18K0170) and
580 NASA New Investigator Program (NNX16AI56G), and USDA NIFA Program. K.G. and C.F.
581 have been supported by the NASA Terrestrial Ecosystem Program through the Carbon Cycle
582 Science Program (NNX17AE14G).

583

584 **References:**

585 Baret, F., Weiss, M., Lacaze, R., Camacho, F., Makmara, H., Pacholczyk, P., Smets, B. 2013.
586 GeoV1: LAI, FAPAR Essential Climate Variables and FCOVER global time series
587 capitalizing over existing products. Part 1: Principles of development and production.
588 Remote Sensing of Environment, 137, 299–309. <https://doi.org/10.1016/j.rse.2012.12.027>
589 Beer, C., Reichstein, M., Tomelleri, E., Ciais, P., Jung, M., Carvalhais, N., Rodenbeck, C., Arain,
590 M.A., Baldocchi, D., Bonan, G.B., Bondeau, A., Cescatti, A., Lasslop, G., Lindroth, A.,
591 Lomas, M., Luysaert, S., Margolis, H., Oleson, K.W., Rouspard, O., Veenendaal, E.,
592 Viovy, N., Williams, C., Woodward, F.I., Papale, D., 2010. Terrestrial Gross Carbon
593 Dioxide Uptake: Global Distribution and Covariation with Climate. Science. 329, 834–
594 838. <https://doi.org/10.1126/science.1184984>
595 Cendrero-mateo, M.P., Carmo-silva, A.E., Porcar-castell, A., Hamerlynck, E.P., Papuga, S.A.,
596 Moran, M.S., 2015. Dynamic response of plant chlorophyll fluorescence to light , water
597 and nutrient availability. Functional Plant Biology. 42, 746-757.
598 <https://doi.org/10.1071/FP15002>

599 Colombo, R., Celesti, M., Bianchi, R., Campbell, P.K.E., Cogliati, S., Cook, B.D., Corp, L.A.,
600 Damm, A., Domec, J.C., Guanter, L., Julitta, T., Middleton, E.M., Noormets, A., Panigada,
601 C., Pinto, F., Rascher, U., Rossini, M., Schickling, A., 2018. Variability of sun-induced
602 chlorophyll fluorescence according to stand age-related processes in a managed loblolly
603 pine forest. *Glob. Chang. Biol.* 24, 2980–2996. <https://doi.org/10.1111/gcb.14097>

604 Daly, C., Halbleib, M., Smith, J.I., Gibson, W.P., Doggett, M.K., Taylor, G.H., Curtis, J., and
605 Pasteris, P.A., 2008. Physiographically-sensitive mapping of temperature and precipitation
606 across the conterminous United States. *International Journal of Climatology*, 28, 2031-
607 2064. <https://doi.org/10.1002/joc.1688>

608 Damm, A., Erler, A., Gioli, B., Hamdi, K., Hutjes, R., Kosvancova, M., et al. (2010). Remote
609 sensing of sun induced fluorescence yield to improve modelling of diurnal courses of gross
610 primary production (GPP). *Global Change Biology*, 16, 171–186.
611 <https://doi.org/10.1111/j.1365-2486.2009.01908.x>

612 Damm, A., Guanter, L., Paul-Limoges, E., van der Tol, C., Hueni, A., Buchmann, N., Eugster,
613 W., Ammann, C., Schaepman, M.E., 2015. Far-red sun-induced chlorophyll fluorescence
614 shows ecosystem-specific relationships to gross primary production: An assessment based
615 on observational and modeling approaches. *Remote Sensing of Environment* 166, 91-
616 105. <https://doi.org/10.1016/j.rse.2015.06.004>

617 Diana, R., Debra, P., William, K., 2000. Changes in grassland canopy structure across a
618 precipitation gradient. *J. Veg. Sci.* 11, 359–368. <https://doi.org/10.2307/3236628>

619 Du, S., Liu, L., Liu, X., Hu, J., 2017. Response of Canopy Solar-Induced Chlorophyll
620 Fluorescence to the Absorbed Photosynthetically Active Radiation Absorbed by
621 Chlorophyll. *Remote Sens.* 9, 911. <https://doi.org/10.3390/rs9090911>

622 Duveiller, G., Cescatti, A., 2016. Remote Sensing of Environment Spatially downscaling sun-
623 induced chlorophyll fluorescence leads to an improved temporal correlation with gross
624 primary productivity. *Remote Sens. Environ.* 182, 72–89.
625 <https://doi.org/10.1016/j.rse.2016.04.027>

626 Flexas, J., Mariano Escalona, J., Evain, S., Gulías, J., Moya, I., Barry Osmond, C., Medrano,
627 H., 2002. Steady-state chlorophyll fluorescence (fs) measurements as a tool to
628 follow variations of net CO₂ assimilation and stomatal conductance during water-stress in

629 c3 plants. *Physiologia Plantarum*. 114, 231–240. <https://doi.org/10.1034/j.1399->
630 3054.2002.1140209.x

631 Fournier, A., Daumard, F., Champagne, S., Ounis, A., Goulas, Y., Moya, I., 2012. Effect of
632 canopy structure on sun-induced chlorophyll fluorescence. *ISPRS Journal of*
633 *Photogrammetry and Remote Sensing* 68, 112-120.
634 <https://doi.org/10.1016/j.isprsjprs.2012.01.003>

635 Frankenberg, C., Berry, J., 2018. Solar Induced Chlorophyll Fluorescence: Origins, Relation to
636 Photosynthesis and Retrieval. *Comprehensive Remote Sensing*. Elsevier. 1986, 143-162
637 <https://doi.org/10.1016/B978-0-12-409548-9.10632-3>

638 Frankenberg, C., Dell, C.O., Berry, J., Guanter, L., Joiner, J., Köhler, P., Pollock, R., Taylor,
639 T.E., 2014. Prospects for chlorophyll fluorescence remote sensing from the Orbiting
640 Carbon Observatory-2. *Remote Sens. Environ.* 147, 1–12.
641 <https://doi.org/10.1016/j.rse.2014.02.007>

642 Frankenberg, C., Fisher, J.B., Worden, J., Badgley, G., Saatchi, S.S., Lee, J.E., Toon, G.C., Butz,
643 A., Jung, M., Kuze, A., Yokota, T., 2011. New global observations of the terrestrial carbon
644 cycle from GOSAT: Patterns of plant fluorescence with gross primary productivity.
645 *Geophys. Res. Lett.* 38, 1–6. <https://doi.org/10.1029/2011GL048738>

646 Gentine, P., Alemohammad, S.H., 2018. Reconstructed Solar-Induced Fluorescence: A Machine
647 Learning Vegetation Product Based on MODIS Surface Reflectance to Reproduce GOME-
648 2 Solar-Induced Fluorescence. *Geophys. Res. Lett.* 45, 3136–3146.
649 <https://doi.org/10.1002/2017GL076294>

650 Guan, K., Berry, J.A., Zhang, Y., Joiner, J., Guanter, L., Badgley, G., Lobell, D.B., 2016.
651 Improving the monitoring of crop productivity using spaceborne solar-induced
652 fluorescence. *Glob. Chang. Biol.* 22, 716–726. <https://doi.org/10.1111/gcb.13136>

653 Guanter, L., Aben, I., Tol, P., Krijger, J.M., Hollstein, A., Köhler, P., Damm, A., Joiner, J.,
654 Frankenberg, C., 2015. Potential of the TROPOspheric Monitoring Instrument
655 (TROPOMI) onboard the Sentinel-5 Precursor for the monitoring of terrestrial chlorophyll
656 fluorescence. *Atmos. Meas. Tech.*, 8, 1337–1352. <https://doi.org/10.5194/amt-8-1337->
657 2015

658 Guanter, L., Frankenberg, C., Dudhia, A., Lewis, P.E., Gómez-dans, J., Kuze, A., Suto, H.,

659 Grainger, R.G., 2012. Retrieval and global assessment of terrestrial chlorophyll fl
660 uorescence from GOSAT space measurements. *Remote Sens. Environ.* 121, 236–251.
661 <https://doi.org/10.1016/j.rse.2012.02.006>

662 Guanter, L., Zhang, Y., Jung, M., Joiner, J., Voigt, M., Berry, J.A., Frankenberg, C., Huete, A.R.,
663 Zarco-Tejada, P., Lee, J.-E., Moran, M.S., Ponce-Campos, G., Beer, C., Camps-Valls, G.,
664 Buchmann, N., Gianelle, D., Klumpp, K., Cescatti, A., Baker, J.M., Griffis, T.J., 2014.
665 Global and time-resolved monitoring of crop photosynthesis with chlorophyll
666 fluorescence. *Proc. Natl. Acad. Sci.* 111, E1327–E1333.
667 <https://doi.org/10.1073/pnas.1320008111>

668 Holder, C.D., 2012. The relationship between leaf hydrophobicity , water droplet retention ,
669 and leaf angle of common species in a semi-arid region of the western United States. *Agric.*
670 *For. Meteorol.* 152, 11–16. <https://doi.org/10.1016/j.agrformet.2011.08.005>

671 Homer, C., Dewitz, J., Yang, L., Jin, S., Danielson, P., Xian, G., Coulston, J., Herold, N.,
672 Wickham, J., Megown, K., 2015. Completion of the 2011 National Land Cover Database
673 for the Conterminous United States – Representing a Decade of Land Cover Change
674 Information. *Photogrammetric Engineering and Remote Sensing*, 81, 345-354.
675 <https://doi.org/10.14358/PERS.81.5.345>

676 Joiner, J., Guanter, L., Lindstrot, R., Voigt, M., Vasilkov, A.P., Middleton, E.M., Huemmrich,
677 K.F., Yoshida, Y., Frankenberg, C., 2013. Global monitoring of terrestrial chlorophyll
678 fluorescence from moderate-spectral-resolution near-infrared satellite measurements:
679 methodology, simulations, and application to GOME-2. *Atmos. Meas. Tech.* 6, 2803–2823.
680 <https://doi.org/10.5194/amt-6-2803-2013>

681 Joiner, J., Yoshida, Y., Vasilkov, A.P., Middleton, E.M., Campbell, P.K.E., Yoshida, Y., Kuze,
682 A., Corp, L.A., 2012. Filling-in of near-infrared solar lines by terrestrial fluorescence and
683 other geophysical effects: Simulations and space-based observations from SCIAMACHY
684 and GOSAT. *Atmos. Meas. Tech.* 5, 809–829. <https://doi.org/10.5194/amt-5-809-2012>

685 Joiner, J., Yoshida, Y., Vasilkov, A.P., Yoshida, Y., Corp, L.A., Middleton, E.M., 2011. First
686 observations of global and seasonal terrestrial chlorophyll fluorescence from space.
687 *Biogeosciences* 8, 637–651. <https://doi.org/10.5194/bg-8-637-2011>

688 Joo, E., Hussain, M.Z., Zeri, M., Masters, M.D., Miller, J.N., Gomez-casanovas, N., Delucia,

689 E.H., 2016. The influence of drought and heat stress on long-term carbon fluxes of
690 bioenergy crops grown in the Midwestern USA. *Plant Cell Environ.* 39, 1928–1940.
691 <https://doi.org/10.1111/pce.12751>

692 Khatami, R., & Mountrakis, G. (2012). Implications of classification of methodological
693 decisions in flooding analysis from hurricane Katrina. *Remote Sensing*, 4(12), 3877–3891

694 Kobayashi, H., Iwabuchi, H., 2008. A coupled 1-D atmosphere and 3-D canopy radiative
695 transfer model for canopy reflectance, light environment, and photosynthesis simulation
696 in a heterogeneous landscape. *Remote Sensing of Environment*, 112, 173–185.
697 <https://doi.org/10.1016/j.rse.2007.04.010>

698 Köhler, P., Frankenberg, C., Magney, T.S., Guanter, L., Joiner, J., Landgraf, J., 2018. Global
699 retrievals of solar induced chlorophyll fluorescence with TROPOMI: first results and inter-
700 sensor comparison to OCO-2. *Geophys. Res. Lett.* 45, 456–463.
701 <https://doi.org/10.1029/2018GL079031>

702 Köhler, P., Guanter, L., Joiner, J., 2015. A linear method for the retrieval of sun-induced
703 chlorophyll fluorescence from GOME-2 and SCIAMACHY data. *Atmos. Meas. Tech.* 8,
704 2589–2608. <https://doi.org/10.5194/amt-8-2589-2015>

705 Li, X., Xiao, J., 2019. A Global, 0.05-Degree Product of Solar-Induced Chlorophyll
706 Fluorescence Derived from OCO-2, MODIS, and Reanalysis Data. *Remote Sens.* 11, 517.
707 <https://doi.org/10.3390/rs11050517>

708 Li, X., Xiao, J., He, B., 2018a. Chlorophyll fluorescence observed by OCO-2 is strongly related
709 to gross primary productivity estimated from flux towers in temperate forests. *Remote*
710 *Sens. Environ.* 204, 659–671. <https://doi.org/10.1016/j.rse.2017.09.034>

711 Li, X., Xiao, J., He, B., 2018b. Higher absorbed solar radiation partly offset the negative effects
712 of water stress on the photosynthesis of Amazon forests during the 2015 drought. *Environ.*
713 *Res. Lett.* 13, 044005. <https://doi.org/10.1088/1748-9326/aab0b1>

714 Li, X., Xiao, J., He, B., Altaf Arain, M., Beringer, J., Desai, A.R., Emmel, C., Hollinger, D.Y.,
715 Krasnova, A., Mammarella, I., Noe, S.M., Ortiz, P.S., Rey-Sanchez, A.C., Rocha, A. V.,
716 Varlagin, A., 2018c. Solar-induced chlorophyll fluorescence is strongly correlated with
717 terrestrial photosynthesis for a wide variety of biomes: First global analysis based on
718 OCO-2 and flux tower observations. *Glob. Chang. Biol.* 24, 3990–4008.

719 <https://doi.org/10.1111/gcb.14297>

720 Liu, X., Guanter, L., Liu, L., Damm, A., Malenovsky, Z., Rascher, U., Peng, D., Du, S.,
721 Gastellu-Etchegorry, J.P., 2018. Downscaling of solar-induced chlorophyll fluorescence
722 from canopy level to photosystem level using a random forest model. *Remote Sens.*
723 *Environ.* <https://doi.org/10.1016/j.rse.2018.05.035>

724 Lu, X., Cheng, X., Li, X., Tang, J., 2018. Opportunities and challenges of applications of
725 satellite-derived sun-induced fluorescence at relatively high spatial resolution. *Sci. Total*
726 *Environ.* 619–620, 649–653. <https://doi.org/10.1016/j.scitotenv.2017.11.158>

727 MacBean, N., Maignan, F., Bacour, C., Lewis, P., Peylin, P., Guanter, L., Köhler, P., Gómez-
728 Dans, J., Disney, M., 2018. Strong constraint on modelled global carbon uptake using
729 solar-induced chlorophyll fluorescence data. *Sci. Rep.* 8, 1–12.
730 <https://doi.org/10.1038/s41598-018-20024-w>

731 Miao, G., Guan, K., Yang, X., Bernacchi, C.J., Berry, J.A., DeLucia, E.H., Wu, J., Moore, C.E.,
732 Meacham, K., Cai, Y., Peng, B., Kimm, H., Masters, M.D., 2018. Sun-Induced
733 Chlorophyll Fluorescence, Photosynthesis, and Light Use Efficiency of a Soybean Field
734 from Seasonally Continuous Measurements. *J. Geophys. Res. Biogeosciences* 123, 610–
735 623. <https://doi.org/10.1002/2017JG004180>

736 Migliavacca, M., Perez-Priego, O., Rossini, M., El-Madany, T.S., Moreno, G., van der Tol, C.,
737 Rascher, U., Berninger, A., Bessenbacher, V., Burkart, A., Carrara, A., Fava, F., Guan, J.H.,
738 Hammer, T.W., Henkel, K., Juarez-Alcalde, E., Julitta, T., Kolle, O., Martín, M.P., Musavi,
739 T., Pacheco-Labrador, J., Pérez-Burgueño, A., Wutzler, T., Zaehle, S., Reichstein, M., 2017.
740 Plant functional traits and canopy structure control the relationship between
741 photosynthetic CO₂ uptake and far-red sun-induced fluorescence in a Mediterranean
742 grassland under different nutrient availability. *New Phytol.* 214, 1078–1091.
743 <https://doi.org/10.1111/nph.14437>

744 Monteith, J.L., 1972. Solar Radiation and Productivity in Tropical Ecosystems. *J. Appl. Ecol.*
745 9, 747. <https://doi.org/10.2307/2401901>

746 Myneni, R., Hoffman, Y., Knyazikhin, 2002. Global products of vegetation leaf area and
747 fraction absorbed PAR from one year of MODIS data. *Remote Sensing of Environment*
748 76, 139–155. [https://doi.org/10.1016/S0034-4257\(02\)00074-3](https://doi.org/10.1016/S0034-4257(02)00074-3)

749 Myneni, R., Knyazkhin, Y. (2018). VIIRS/NPP Leaf Area Index/FPAR 8-Day L4 Global 500m
750 SIN Grid V001 [Data set]. NASA EOSDIS Land Processes DAAC. doi:
751 10.5067/VIIRS/VNP15A2H.001

752 Ollinger, S. V., Richardson, A. D., Martin, M. E., Hollinger, D. Y., Frolking, S. E., Reich, P.
753 B., et al. (2008). Canopy nitrogen, carbon assimilation, and albedo in temperate and
754 boreal forests: Functional relations and potential climate feedbacks. *Proceedings of*
755 *the National Academy of Sciences of the United States of America*, 105, 19336–19341.

756 Oosterhuis, D.M., Walker, S., Eastham, J., 1985. Soybean Leaflet Movements as an Indicator
757 of Crop Water Stress. *Crop Science*. 25, 1101–1106.
758 <https://doi.org/10.2135/cropsci1985.0011183X002500060048x>

759 Peng, D., Zhang, B., Liu, L., Fang, H., Chen, D., Hu, Y., Liu, L., 2012. Characteristics and
760 drivers of global NDVI-based FPAR from 1982 to 2006 26, 1–15.
761 <https://doi.org/10.1029/2011GB004060>

762 Porcar-castell, A., Tyystjärvi, E., Atherton, J., Tol, C. Van Der, Flexas, J., Pfündel, E.E., Moreno,
763 J., Frankenberg, C., Berry, J.A., 2014. Linking chlorophyll a fluorescence to
764 photosynthesis for remote sensing applications: mechanisms and challenges 65, 4065–
765 4095. <https://doi.org/10.1093/jxb/eru191>

766 Romero, J.M., Cordon, G.B., Lagorio, M.G., 2018. Modeling re-absorption of fluorescence
767 from the leaf to the canopy level. *Remote Sens. Environ.* 204, 138–146.
768 <https://doi.org/10.1016/j.rse.2017.10.035>

769 Ryu, Y., Jiang, C., Kobayashi, H., Detto, M., 2018. MODIS-derived global land products of
770 shortwave radiation and diffuse and total photosynthetically active radiation at 5 km
771 resolution from 2000. *Remote Sens. Environ.* 204, 812–825.
772 <https://doi.org/10.1016/j.rse.2017.09.021>

773 Shiga, Y.P., Tadić, J.M., Qiu, X., Yadav, V., Andrews, A.E., Berry, J.A., Michalak, A.M., 2018.
774 Atmospheric CO₂ observations reveal strong correlation between regional net biospheric
775 carbon uptake and solar-induced chlorophyll fluorescence. *Geophys. Res. Lett.* 45, 1122–
776 1132. <https://doi.org/10.1002/2017GL076630>

777 Smith, W.K., Biederman, J.A., Scott, R.L., Moore, D.J.P., He, M., Kimball, J.S., Yan, D.,
778 Hudson, A., Barnes, M.L., MacBean, N., Fox, A.M., Litvak, M.E., 2018. Chlorophyll
779 Fluorescence Better Captures Seasonal and Interannual Gross Primary Productivity

780 Dynamics Across Dryland Ecosystems of Southwestern North America. *Geophys. Res.*
781 *Lett.* 45, 748–757. <https://doi.org/10.1002/2017GL075922>

782 Song, L., Guanter, L., Guan, K., You, L., Huete, A., Ju, W., Zhang, Y., 2018. Satellite sun-
783 induced chlorophyll fluorescence detects early response of winter wheat to heat stress in
784 the Indian Indo-Gangetic Plains. *Glob. Chang. Biol.* 24, 4023–4037.
785 <https://doi.org/10.1111/gcb.14302>

786 Sun, Y., Frankenberg, C., Jung, M., Joiner, J., Guanter, L., Köhler, P., Magney, T., 2018.
787 Overview of Solar-Induced chlorophyll Fluorescence (SIF) from the Orbiting Carbon
788 Observatory-2: Retrieval, cross-mission comparison, and global monitoring for GPP.
789 *Remote Sens. Environ.* 209, 808–823. <https://doi.org/10.1016/j.rse.2018.02.016>

790 Sun, Y., Fu, R., Dickinson, R., Joiner, J., Frankenberg, C., Gu, L., Xia, Y., Fernando, N., 2015.
791 Drought onset mechanisms revealed by satellite solar-induced chlorophyll fluorescence:
792 Insights from two contrasting extreme events. *J. Geophys. Res. Biogeosciences* 120,
793 2427–2440. <https://doi.org/10.1002/2015JG003150>

794 Suyker, A.E., Verma, S.B., 2012. Gross primary production and ecosystem respiration of
795 irrigated and rainfed maize – soybean cropping systems over 8 years. *Agricultural and*
796 *Forest Meteorology.* 165, 12–24. <https://doi.org/10.1016/j.agrformet.2012.05.021>

797 Tian, Y., 2004. Comparison of seasonal and spatial variations of leaf area index and fraction of
798 absorbed photosynthetically active radiation from Moderate Resolution Imaging
799 Spectroradiometer (MODIS) and Common Land Model. *J. Geophys. Res.* 109, D01103.
800 <https://doi.org/10.1029/2003JD003777>

801 USDA Foreign Agricultural Service (December 2018) World Agricultural Production, Circular
802 Ser WAP 12-18, pp. 17-24.

803 Verma, M., Schimel, D., Evans, B., Frankenberg, C., Beringer, J., Drewry, D.T., Magney, T.,
804 Marang, I., Hutley, L., Moore, C., Eldering, A., 2017. Effect of environmental conditions
805 on the relationship between solar-induced fluorescence and gross primary productivity at
806 an OzFlux grassland site. *J. Geophys. Res. Biogeosciences* 122, 716–733.
807 <https://doi.org/10.1002/2016JG003580>

808 Verrelst, J., Rivera, J.P., van der Tol, C., Magnani, F., Mohammed, G., Moreno, J., 2015. Global
809 sensitivity analysis of the SCOPE model: What drives simulated canopy-leaving sun-

810 induced fluorescence? *Remote Sens. Environ.* 166, 8–21.
811 <https://doi.org/10.1016/j.rse.2015.06.002>

812 Wang, C., Chen, J., Wu, J., Tang, Y., Shi, P., Black, T.A., Zhu, K., 2017. A snow-free vegetation
813 index for improved monitoring of vegetation spring green-up date in deciduous
814 ecosystems. *Remote Sens. Environ.* 196, 1–12. <https://doi.org/10.1016/j.rse.2017.04.031>

815 Wood, J.D., Griffis, T.J., Baker, J.M., Frankenberg, C., Verma, M., Yuen, K., 2017. Multiscale
816 analyses of solar-induced fluorescence and gross primary production. *Geophys. Res. Lett.*
817 44, 533–541. <https://doi.org/10.1002/2016GL070775>

818 Xu, S., Liu, Z., Zhao, L., Zhao, H., Ren, S., 2018. Diurnal response of sun-induced fluorescence
819 and PRI to water stress in maize using a near-surface remote sensing platform. *Remote*
820 *Sens.* 10, 1510. <https://doi.org/10.3390/rs10101510>

821 Yan, K., Park, T., Yan, G., Liu, Z., Yang, B., Chen, C., Nemani, R.R., Knyazikhin, Y., Myneni,
822 R.B., 2016. Evaluation of MODIS LAI / FPAR Product Collection 6 . Part 2 : Validation
823 and Intercomparison. *Remote Sens.* 8, 460. <https://doi.org/10.3390/rs8060460>

824 Yang, H., Yang, X., Zhang, Y., Heskell, M.A., Lu, X., Munger, J.W., Sun, S., Tang, J., 2017.
825 Chlorophyll fluorescence tracks seasonal variations of photosynthesis from leaf to canopy
826 in a temperate forest. *Glob. Chang. Biol.* 23, 2874–2886.
827 <https://doi.org/10.1111/gcb.13590>

828 Yang, K., Ryu, Y., Dechant, B., Berry, J.A., Hwang, Y., Jiang, C., Kang, M., Kim, J., Kimm, H.,
829 Kornfeld, A., Yang, X., 2018. Sun-induced chlorophyll fluorescence is more strongly
830 related to absorbed light than to photosynthesis at half-hourly resolution in a rice paddy.
831 *Remote Sens. Environ.* 216, 658–673. <https://doi.org/10.1016/j.rse.2018.07.008>

832 Yang, P., van der Tol, C., 2018. Linking canopy scattering of far-red sun-induced chlorophyll
833 fluorescence with reflectance. *Remote Sens. Environ.* 209, 456–467.
834 <https://doi.org/10.1016/j.rse.2018.02.029>

835 Yang, X., Tang, J., Mustard, J.F., Lee, J., Rossini, M., 2015. Solar-induced chlorophyll
836 fluorescence correlates with canopy photosynthesis on diurnal and seasonal scales in a
837 temperate deciduous forest. *Geophys. Res. Lett.* 42, 2977–2987.
838 <https://doi.org/10.1002/2015GL063201>

839 Yoshida, Y., Joiner, J., Tucker, C., Berry, J., Lee, J.E., Walker, G., Reichle, R., Koster, R.,

840 Lyapustin, A., Wang, Y., 2015. The 2010 Russian drought impact on satellite
841 measurements of solar-induced chlorophyll fluorescence: Insights from modeling and
842 comparisons with parameters derived from satellite reflectances. *Remote Sens. Environ.*
843 166, 163–177. <https://doi.org/10.1016/j.rse.2015.06.008>

844 Zeng, Y., Badgley, G., Dechant, B., Ryu, Y., Chen, M., Berry, J.A., 2019. A practical approach
845 for estimation the escape ratio of near-infrared solar-induced chlorophyll fluorescence.
846 *Remote Sens. Environ.* 232, 111209. <https://doi.org/10.1016/j.rse.2019.05.028>

847 Zhang, Y., Guanter, L., Berry, J.A., Joiner, J., van der Tol, C., Huete, A., Gitelson, A., Voigt, M.,
848 Köhler, P., 2014. Estimation of vegetation photosynthetic capacity from space-based
849 measurements of chlorophyll fluorescence for terrestrial biosphere models. *Glob. Chang.*
850 *Biol.* 20, 3727–3742. <https://doi.org/10.1111/gcb.12664>

851 Zhang, Y., Guanter, L., Berry, J.A., van der Tol, C., Yang, X., Tang, J., Zhang, F., 2016. Model-
852 based analysis of the relationship between sun-induced chlorophyll fluorescence and gross
853 primary production for remote sensing applications. *Remote Sens. Environ.* 187, 145–155.
854 <https://doi.org/10.1016/j.rse.2016.10.016>

855 Zhang, Y., Joiner, J., Alemohammad, S.H., Zhou, S., Gentine, P., 2018. A global spatially
856 Continuous Solar Induced Fluorescence (CSIF) dataset using neural networks.
857 *Biogeosciences* 15, 5779–5800. <https://doi.org/10.5194/bg-15-5779-2018>

858 Zhang, Z., Zhang, Y., Joiner, J., Migliavacca, M., 2018. Angle matters : Bidirectional effects
859 impact the slope of relationship between gross primary productivity and sun - induced
860 chlorophyll fluorescence from Orbiting Carbon Observatory - 2 across biomes. *Global*
861 *Biogeochem. Cycles* 24, 5017–5020. <https://doi.org/10.1111/gcb.14427>

862 Zuromski, L.M., Bowling, D.R., Köhler, P., Frankenberg, C., Goulden, M.L., Blanken, P.D.,
863 Lin, J.C., 2018. Solar-Induced Fluorescence Detects Interannual Variation in Gross
864 Primary Production of Coniferous Forests in the Western United States. *Geophys. Res.*
865 *Lett.* 45, 7184–7193. <https://doi.org/10.1029/2018GL077906>

866

867 **Glossary:**

868 SIF: solar-induced chlorophyll fluorescence

869 SIF_{inst} : instantaneous solar-induced chlorophyll fluorescence

870 SIF_{par} : SIF_{inst} normalized by PAR

871 $SIF_{yield\ apparent}$: apparent canopy SIF yield, defined as SIF observed in the direction of the

872 sensor per PAR absorbed by canopies, is a product of fluorescence yield and the escaping

873 ratio.

874 Φ_F : fluorescence yield

875 f^{esc} : the escaping ratio, which can be calculated as $NIR_v/fPAR$

876 GPP: gross primary production

877 LUE: light use efficiency of GPP

878 PAR: photosynthetically active radiation

879 fPAR: the fraction of absorbed photosynthetically active radiation

880 APAR: absorbed photosynthetically active radiation

881 NIR_v : the near-infrared reflectance of vegetation, which can be calculated as $NDVI * NIR$

882 NIR: the reflectance of near-infrared band

883 NDVI: normalized difference vegetation index

884 LAI: leaf area index

885 LAD: leaf angle distribution

886

Supplementary Data

[Click here to download Supplementary Data: Supporting Information.docx](#)

Declaration of interests

The authors declare that they have no known competing financial interests or personal relationships that could have appeared to influence the work reported in this paper.

The authors declare the following financial interests/personal relationships which may be considered as potential competing interests:

Cong Wang: Conceptualization, Methodology, Software, Formal analysis, Investigation, Writing - Original Draft, Writing – Review & Editing, Visualization. **Kaiyu Guan:** Conceptualization, Methodology, Writing - Original Draft, Writing – Review & Editing, Supervision, Funding acquisition. **Bin Peng:** Conceptualization, Methodology, Writing - Original Draft, Writing – Review & Editing. **Min Chen:** Conceptualization, Writing - Original Draft. **Chongya Jiang:** Writing - Original Draft, Writing – Review & Editing. **Yelu Zeng:** Methodology, Writing – Review & Editing. **Genghong Wu:** Formal analysis, Writing – Review & Editing. **Sheng Wang:** Writing – Review & Editing. **Jin Wu:** Conceptualization, Writing - Original Draft. **Xi Yang:** Writing - Original Draft, Writing. **Christian Frankenberg:** Resource, Writing - Original Draft. **Philipp Köhler:** Resource, Writing - Original Draft. **Joseph Berry:** Conceptualization. **Carl Bernacchi:** Writing - Original Draft. **Kai Zhu:** Writing - Original Draft. **Caroline Alden:** Writing - Original Draft, Writing – Review & Editing. **Guofang Miao:** Conceptualization.